

Lawrence Berkeley National Laboratory

Lawrence Berkeley National Laboratory

Title

Measuring and modeling fault density for CO2 storage plume fault encounter probability estimation

Permalink

<https://escholarship.org/uc/item/2254r5m7>

Author

Jordan, P.D.

Publication Date

2013-01-15

Peer reviewed

Measuring and modeling fault density for CO₂ storage plume-fault encounter probability estimation

Preston D. Jordan, Curtis M. Oldenburg,
and Jean-Philippe Nicot

ABSTRACT

Emission of carbon dioxide (CO₂) from fossil-fueled power generation stations contributes to global climate change. Capture of CO₂ from such stationary sources and storage within the pores of geologic strata (geologic carbon storage) is one approach to mitigating anthropogenic climate change. The large storage volume needed for this approach to be effective requires injection into pore space saturated with saline water in reservoir strata overlain by cap rocks. One of the main concerns regarding storage in such rocks is leakage via faults. Such leakage requires, first, that the CO₂ plume encounter a fault and, second, that the properties of the fault allow CO₂ to flow upward. Considering only the first step of encounter, fault population statistics suggest an approach to calculate the probability of a plume encountering a fault, particularly in the early site-selection stage when site-specific characterization data may be lacking. The resulting fault encounter probability approach is applied to a case study in the southern part of the San Joaquin Basin, California. The CO₂ plume from a previously planned injection was calculated to have a 4.1% chance of encountering a fully seal offsetting fault and a 9% chance of encountering a fault with a throw half the seal thickness. Subsequently available information indicated the presence of a half-seal offsetting fault at a location 2.8 km (1.7 mi) northeast of the injection site. The encounter probability for a plume large enough to encounter a fault with this throw at this distance from the injection site is 25%, providing a single before and after test of the encounter probability estimation method.

ACKNOWLEDGEMENTS

We thank Chris Doughty (Lawrence Berkeley National Laboratory) for sharing the pilot test simulation results and Jeff Wagoner (Lawrence Livermore National Laboratory) for sharing his expertise regarding the geology of the southern San Joaquin Valley, particularly in the vicinity of the pilot test site. We also thank Tiemi Onishi for providing an internal review and for suggesting that the study could be reported in two papers to provide the space necessary to properly convey it. We thank all of the peer reviewers that offered comments, particularly Nancye H. Dawers. After voluntarily identifying herself, she offered constructive reviews that were far beyond the norm. In addition, we thank AAPG consulting editor Frances Plant Whitehurst for her keen input on several technical and editorial issues, which led to considerable further improvement. Of course, none of the above should be construed as indicating that the authors take anything other than full responsibility for the data analysis and conclusions presented. This work was supported in part by the CO₂ Capture Project of the Joint Industry Program and by the Lawrence Berkeley National Laboratory under U.S. Department of Energy contract no. DE-AC02-05CH11231.

INTRODUCTION

Fossil fuel-fired electrical power plants emitted 40% of the carbon dioxide (CO₂) resulting from energy usage in the United States in 2008 (EIA, 2009). Storage of a part of this CO₂ in the pore space of geologic strata (geologic carbon storage) is one possible mitigation for the part of climate change associated with emitting this pollutant to the atmosphere.

Geologic carbon storage is envisioned in strata from which oil or gas has been produced as well as strata containing primarily saline waters, termed “saline aquifers.” Injection into unminable coal beds to allow adsorption is another option. Estimates indicate that as much as tens of metric Gt of CO₂ per year can feasibly be captured in a few decades time (Gale, 2005). Global total oil and gas field storage capacity is estimated at many hundred to almost a thousand Gt of CO₂ (Benson and Cook, 2005). This suggests that oil and gas fields could provide all the necessary storage.

However, no general tendency exists for large point sources of CO₂ emissions to be located near oil or gas fields. This lack of proximity between sources, for example, large coal-fired power plants, and sinks consisting of oil and gas reservoirs would necessitate extensive CO₂ transportation pipeline networks. However, sedimentary basins with alternating reservoir and cap-rock sequences filled with saline water are amenable to geologic carbon storage and are present under large areas of North America thereby reducing transportation requirements. With large capacity and wide spatial distribution (Benson and Cook, 2005), the focus for large-scale geologic carbon storage that can make a material difference in reducing CO₂ emissions is on saline systems in sedimentary basins.

Even where source and oil and gas field volumes are collocated, storage awaits a field owner deciding that such an activity, even if combined with CO₂-enhanced recovery, would provide the greatest economic return. In contrast, storage in saline aquifers does not have hydrocarbon market timing constraints. For this reason, as well as their greater and more widespread storage capacity, a substantial part of storage will likely need to occur in saline aquifers if carbon capture and storage is to significantly mitigate greenhouse gas emissions.

Leakage of CO₂ out of designated subsurface storage volumes, whether oil and gas fields or saline aquifers, is one of the main concerns regarding geologic carbon storage. Fault zones are considered as one of the main potential leakage pathways (Benson and Cook, 2005). More is generally known about the location and character of faults in a known oil and gas reservoir than in a saline aquifer. Consequently, a more deterministic

assessment of leakage risk caused by faults is possible for storage in mature oil and gas reservoirs, and a more probabilistic assessment is necessary for saline aquifers in the early site-selection phase of a project.

For leakage via a fault to occur, stored CO₂ must first encounter the fault, and then that fault must be relatively more transmissive than the surrounding rock. This article focuses on a method for estimating the probability of the first of these steps, that is, CO₂ encountering a fault. This article does not consider the second step regarding whether a fault is transmissive if such an encounter occurs.

Two inputs are needed for assessing the fault encounter probability: the plume geometry and fault statistics (Jordan et al., 2011). The necessary fault statistics concern fault strike and density versus size. Numerical modeling can provide realizations of the plume geometry. This article develops a more readily usable fault statistical approach for use in calculating the encounter probability and applies that approach to develop fault statistics from publicly available data to calculate a plume-fault encounter probability for a hypothetical pilot test site in the southeastern San Joaquin Valley, California.

BACKGROUND

Numerous investigators have found that fault length and displacement populations can commonly be represented by a power-law distribution. This finding is based on field research (e.g., Watterson et al., 1996), physical modeling (e.g., Ackermann et al., 2001), and numerical simulations (e.g., Cowie et al., 1995). Power-law distributions are of the form

$$N \propto aS^{-C} \quad (1)$$

where N is the number of faults of a size greater than S , and C is the power-law exponent (notations from Watterson et al., 1996). For instance, N can represent the number of faults greater than a certain length determined from a two-dimensional (2-D) sample space, such as a geologic map. Alternatively, N can represent the number of faults with greater than a certain displacement, d , encountered

in a one-dimensional sample space, such as a scan line. When d (known as the displacement cutoff) is substituted for S , equation 1 becomes

$$N_d \propto d^{-C_d} \quad (2)$$

where the subscript d is for displacement cutoff.

Field studies, numerical simulations, and physical modeling have also indicated that, at very low strains and high strains, fault density versus displacement cutoff is exponential instead of power law (Cowie et al., 1995; Ackermann et al., 2001). They also show that C_d declines with increasing strain during the initiation of faulting and becomes constant with further strain. At initiation of strain, many small faults develop, and so C_d is large. As strain continues, some of the faults grow and eventually link, whereas few new small faults develop, so C_d decreases. Values reported in the literature are likely to emphasize lower values for C_d because field studies are easier to conduct on more heavily faulted terrains. At very high strains, further development of a few faults or even one fault dominates, termed as “characteristic fault(s).” Such populations are marked by an exponential instead of a power-law distribution in the larger fault range (Hardacre and Cowie, 2003).

FAULT DENSITY APPROACH

If N represents the number of faults longer than a certain length, it is commonly difficult to measure in practice because of the confounding effects of fault intersections. Furthermore, the orientation of the boundary of a fault map can introduce scatter in the fault density distribution measured from the map.

The areal density of faults (length per area), F , with a certain value of d is easier to measure. It can be accurately calculated by measuring the length of faults with greater than a certain displacement occurring in a map area and dividing by that area. It avoids handling of fault intersections inherent in defining the number of faults based on length, and it does not suffer from bias introduced by the orientation of map margins. The use of F is workable because it is proportional to N_d , as shown next, and so can be substituted for N_d in equation 2.

N_d can be multiplied by the average length of the fault (l_d) represented by each fault intersection with one of multiple scan lines across a map assuming that the faults have no orientation bias or that the scan lines are randomly oriented. This value is proportional to the average sample-line spacing. Multiplying N_d by l_d yields

$$l_d N_d = L \quad (3)$$

where L is the total length of faults with d greater than a particular value. As the space between the scan lines approaches the limit of 0, equation 3 approaches equality.

L can be directly measured from a fault map instead of through scan lines. Multiplying equation 2 by l_d yields

$$l_d N_d \propto d^{-C_d} \quad (4)$$

Substituting equation 3 into equation 4 and dividing by the total area of the sample domain, A , gives

$$\frac{L}{A} \propto d^{-C_d} \quad (5)$$

The value of L divided by A is the fault density, F , so equation 5 can be rewritten as

$$F \propto d^{-C_d} \quad (6)$$

An additional implication of equation 6 is that F follows the same pattern as N_d as strain accumulates.

Taking the log of equation 6 gives

$$\log F \propto -C_d \log d \quad (7)$$

Equation 7 indicates that a log-log plot of F against d will be linear if the fault population follows a power-law distribution. A semilog plot of F against d will be linear if the distribution is exponential (very early- or late-stage strain).

Equation 7 implies that F approaches infinity as d approaches 0. In practice, most fault population researchers have found, or believe based on theoretical

considerations, that the relationship is accurate down to displacements equivalent to several grain diameters for clastic rocks (e.g., Ackermann et al., 2001). Even this implies that F becomes very large at the actual lower limit of d . This suggests a high probability that a given CO₂ plume will encounter a fault of some size. Of course, most such faults will have such small displacements as to not be of serious concern in terms of leakage. Consequently, the concern for leakage should focus on faults of a certain size (large enough to have a high probability of leakage) instead of on all faults encountered, as is commonly the case currently.

As defined above, F is a measure of fault density in a 2-D space and so is independent of fault dip. As such, F provides a biased estimate of the fault density in the three-dimensional (3-D) rock volume (Pickering et al., 1995). Because of the buoyancy of CO₂, and typically because of the much greater length and width than thickness of most proposed storage reservoirs, CO₂ plumes will typically be more 2-D than 3-D. As a result, F is the proper parameter for estimating the probability of a CO₂ plume encountering a fault with a given displacement.

However, 3-D fault density can enter back into consideration several steps after a plume encounters a fault. After such an encounter, the first issue is the flow and transport properties of the fault. If these properties are such that leakage via the fault can occur, then the next relevant issue is the vertical extent of the part of the fault with these properties. If the extent of this part of the fault is sufficient to allow leakage all the way from the CO₂ plume to a volume of concern (i.e., a receptor such as an underground source of drinking water), then analysis should proceed to the consideration of impacts. If the extent of the leakage-capable part of the fault is insufficient to allow direct leakage to a receptor, but sufficient to allow leakage out of the storage formation, then consideration of leakage via more complex pathways must occur. This network is defined in part by the 3-D fault density, along with the distribution of permeable geologic units in relation to the fault density. Such considerations are outside of this study, but the probability of flow through conductive fault networks with power-law populations is developed by Zhang et al. (2010).

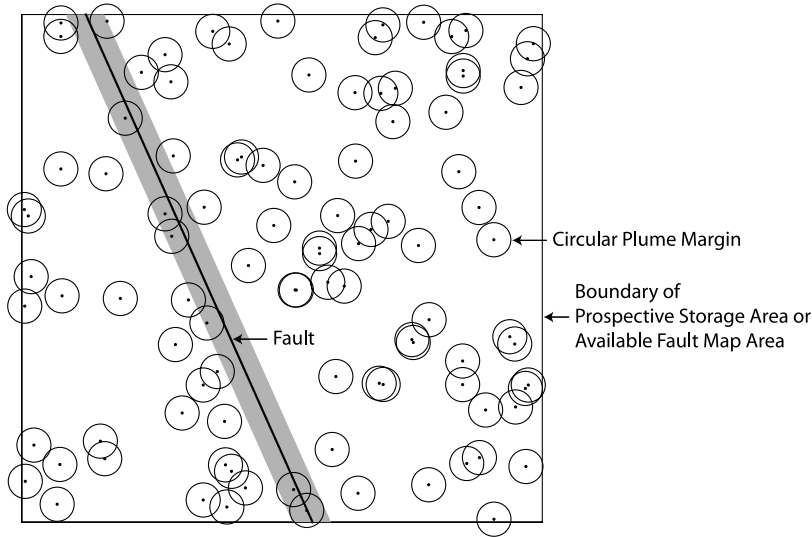


Figure 1. Map view of randomly located circular plumes centered in a prospective storage area or fault map area. Plumes within a radius of an unknown fault, indicated by the gray area, will encounter the fault.

FAULT ENCOUNTER PROBABILITY

For a circular plume in plan to encounter a fault, it must be centered within a radius of either side of the fault. Discounting the ends of the fault, a plume centered within a plume-diameter wide stripe centered on the fault will encounter the fault, as shown in Figure 1. Dividing this area by the study area, such as the part of the basin under consideration for locating a storage project or the available fault map area, gives the probability of a randomly located plume encountering the fault. It also gives the probability of a plume at a known location encountering a randomly located fault of the same length in the study area, again discounting end effects.

The fault stripe area is the plume diameter multiplied by the fault length as shown in Figure 1. The fault length is the fault density multiplied by the study area. So, the study area occurs in both the numerator and the denominator of the probability calculation, leaving just the plume diameter multiplied by the fault density.

This result can be generalized to noncircular areas swept by CO₂. This requires ascertaining the fault strike mode from available fault maps, as well as estimating the expected shape of the sweep area. This shape can be estimated from the numerical simulations of the proposed CO₂ injection.

Taking half the length of the sweep area perpendicular to the fault as λ ,

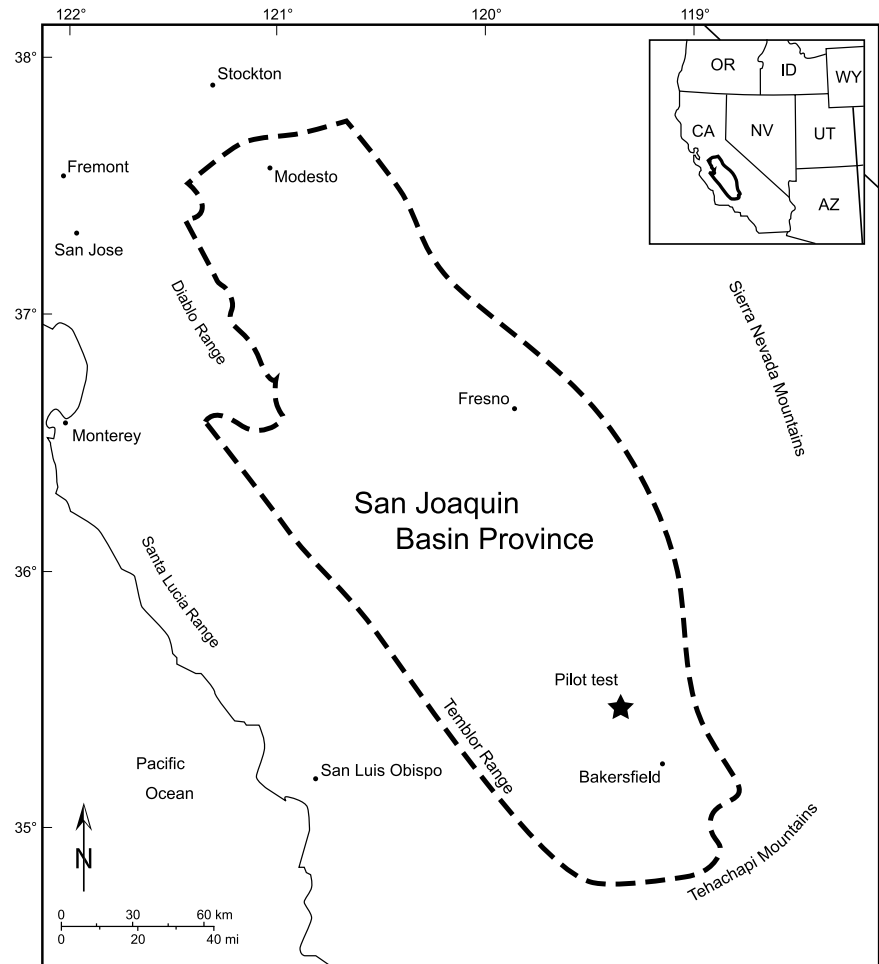
$$\Pr(g) = 2\lambda F \quad (8)$$

where g is the encounter of a fault by a plume, and $\Pr(g)$ is the probability of such an encounter. The half length of the sweep area is used to emphasize that the area must be centered within this distance of a fault for CO₂ to encounter it and that potential faults on either side of the area contribute to the probability. Using the fault-perpendicular dimension of the sweep area in the equation instead, such as the diameter for circular plumes, could lead to misunderstanding. The derivation of equation 8 is further detailed in Jordan et al. (2011).

If more than one fault strike mode is observed, then multiple distributions of F will have to be defined based on measurements from the fault map. Each mode will also require a different λ unless the sweep area is radially symmetric. Equation 8 can then be used to calculate a $\Pr(g)$ for each mode for each fault size of interest.

Equation 8 inherently has several assumptions (Jordan et al., 2011). As mentioned above, it presumes that the region swept can be approximated as a 2-D space to allow the use of aerial instead of volumetric fault density. It also assumes that the plume encounters only one fault. So, the fault-perpendicular dimension of the sweep area must be much less than the likely spacing between the faults of interest. Another way to view this is that, as the fault encounter probability resulting from equation 8 increases, overestimation of the probability increases because of assuming that a plume encounters only one fault.

Figure 2. Location of the previously proposed pilot test in the San Joaquin Basin in California (modified from Scheirer and Magoon, 2007). OR = Oregon; ID = Idaho; WY = Wyoming; CA = California; NV = Nevada; UT = Utah; AZ = Arizona.



This overestimation is negligible at small probabilities. For instance, assuming a random fault distribution and a single fault encounter probability of 5%, the likelihood of encountering two such faults (ignoring fault effects on plume evolution) is just 0.25%.

FAULT ENCOUNTER PROBABILITY ESTIMATION METHOD

Given equation 8, estimating the probability of a CO₂ plume encountering a fault can proceed as follows (Jordan et al., 2011):

1. Identify the fault map(s) relevant to a proposed site.
2. Measure fault lengths, orientations, and displacement profiles from the map(s).
3. Determine fault orientation modes.
4. Analyze spatial trends in the areal fault density (length divided by area), F , and select a data set applicable to the proposed site.
5. Calculate F for faults with displacements greater than a value of interest, d , and plot in log-log and semilog space.
6. Model the F -versus- d distribution.
7. Estimate the length of the plume perpendicular to the faults of interest or estimate the plume area, aspect ratio, and orientation.
8. Calculate the encounter probability at the d of interest from the F -versus- d distribution model, fault orientation modes, and fault-perpendicular plume length.

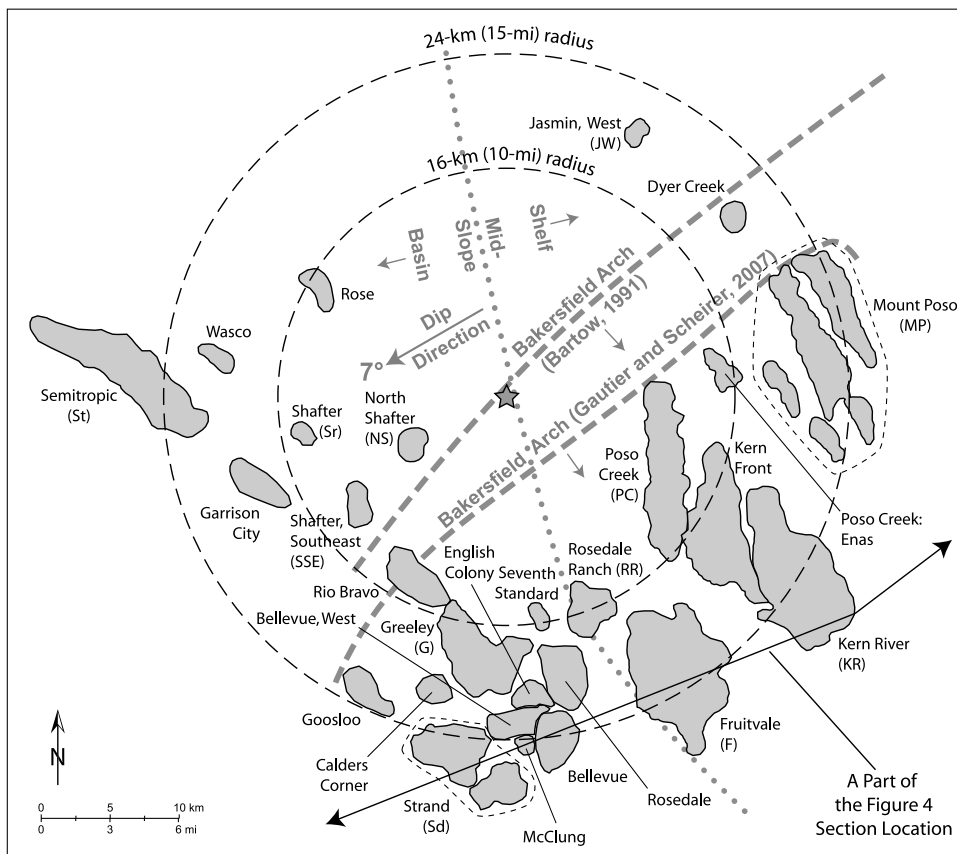


Figure 3. The pilot test site is at the star with nearby oil and gas fields and major depositional environment and structural boundaries shown (depositional environment boundary from Gautier and Scheirer, 2007; dip direction and magnitude from Wagoner, 2009; and oil and gas fields from California Division of Oil, Gas and Geothermal Resources [DOGGR], 1998).

CASE STUDY: SOUTHEASTERN SAN JOAQUIN VALLEY PILOT TEST

A previously planned pilot test site was located in the southeastern part of the San Joaquin Basin in California approximately 27 km (17 mi) northwest of Bakersfield, as shown in Figure 2. This test was to inject 1 Mt (10^6 t = 10^9 kg; 1.1×10^6 T = 2.2×10^9 lb) of CO₂ into a suitable stratum over 4 yr (National Energy Technology Laboratory [NETL], 2009). Planning for the test was terminated when construction of the pilot power plant that was to supply the CO₂ was canceled.

Geologic Setting

The San Joaquin Basin extends approximately 350 km (220 mi) from the Stockton arch in the north to the northern Transverse Ranges in the south and from the Sierra Nevada in the east to the California Coast

Ranges in the west. The San Joaquin Basin averages 80 to 110 km (50–70 mi) wide (National Energy Technology Laboratory [NETL], 2009). During the Mesozoic, the area was a forearc basin during the subduction of the Farallon plate. By the middle Tertiary, the basin had become relatively isolated as a result of the transpressional margin that followed the passage of the Mendocino triple junction. The depositional environment generally progressed from deep marine in the Mesozoic to alluvial at present, with several intervening transgression-regression sequences (Graham and Williams, 1985).

The Vedder Sand consists of interbedded sandstones and shales deposited on the marine slope, shelf, and delta comprising a ramp (Bloch, 1986). The test site is at the boundary of the shelf to upper slope and lower slope to basin depositional environments at the time of deposition of the Vedder as shown in Figure 3 (Gautier and Scheirer, 2007). As shown in Figure 3, the site is structurally either at or just a short distance north of the northern margin of the Bakersfield arch

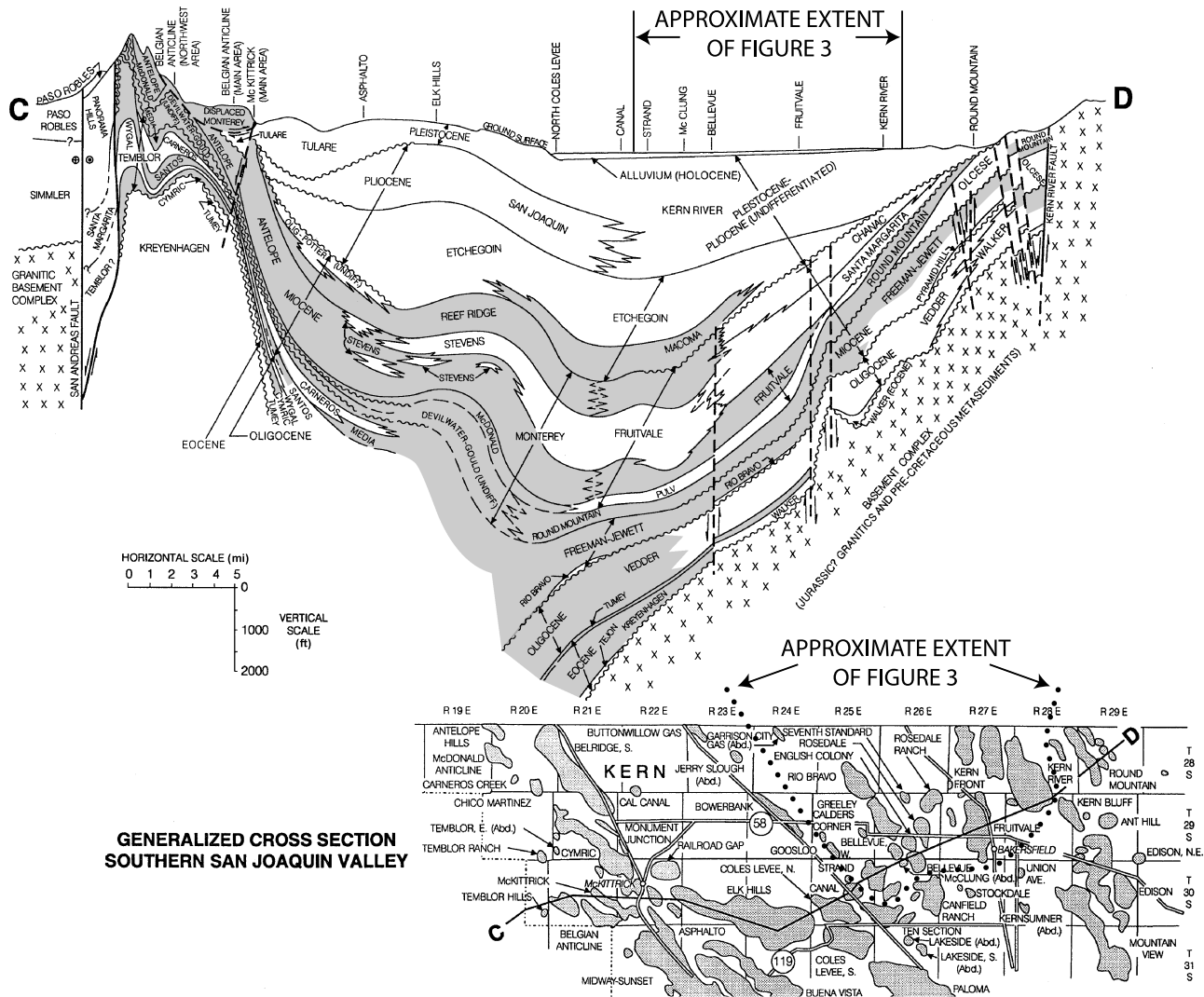


Figure 4. Generalized section for the southeastern San Joaquin Basin (California Division of Oil, Gas and Geothermal Resources [DOGGR], 1998). Oil fields are stippled on the map. Predominantly fine-grained (shale) units without significant coarse-grained reservoirs are shaded gray on the section according to Scheirer and Magoon (2007) with the position of the Freeman and Vedder facies changed based on wireline logs in California Division of Oil, Gas and Geothermal Resources (DOGGR) (1998) and Pulv unit lithology changes based on Callaway (1990).

(Bartow, 1991; Gautier and Scheirer, 2007). The more significant faults in the vicinity appear to extend from the basement to the Miocene–Pliocene unconformity, as shown in Figure 4. These faults appear to be primarily growth faults that are vertical upsection of the Vedder and likely subvertical at the Vedder (McPherson, 1978).

At the site, the Vedder dips 7° to the west southwest, has a thickness of as much as 160 m (520 ft), and occurs at a depth of 2300 m (7500 ft) (Wagoner, 2009). The Freeman Silt provides a good overlying seal at the site and surrounding areas (Wagoner, 2009).

Fault Data

Detailed information on faults at the pilot test site is not available. Twenty-seven oil and gas fields exist wholly or partially within 24 km (15 mi) of the pilot test site as shown in Figure 3. A structure map for each field, mostly showing faults, is publicly available, with the exception of the Rose field for which no data were available (California Division of Oil, Gas and Geothermal Resources [DOGGR], 1998). These maps provide a basis for predicting the fault population in the vicinity of the pilot test site. An example structure map is shown in Figure 5.

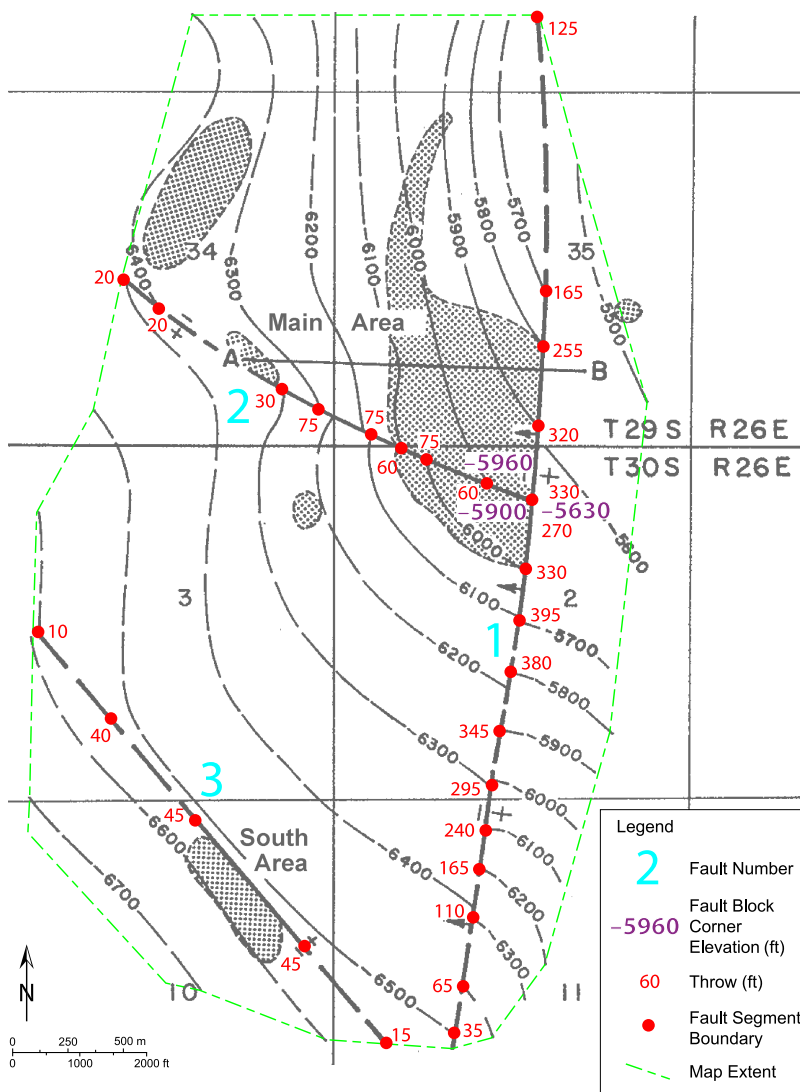


Figure 5. Structure map of the N electric log marker in the Bellevue oil field modified from California Division of Oil, Gas and Geothermal Resources (DOGGR) (1998). The N electric marker occurs near the base of the Reef Ridge Shale. The location of this field and the geologic unit are shown on Figure 4. The stippled areas represent the extent of oil accumulations.

Richardson (1966) also presents a structure map of the top of the Vedder sands based on oil field and exploratory well data. As such, the data density, and so also the map accuracy, vary considerably from within fields to between fields. For instance, the map only shows two wells in the township where the injection site is located and no wells in the next closest township to the injection site, which is to the west.

In addition, the comparison of the Richardson (1966) structure map with the few oil field structure maps on the same surface indicates some significant differences. For instance, Richardson (1966) indicates a maximum of more than 120 m (400 ft) of displacement on the Greeley fault in the Greeley field, whereas the structure map for that field in California Division of Oil, Gas and Geothermal Resources

(DOGGR) (1998) shows approximately 40 m (130 ft) of displacement in the same location.

Based on the data above, the individual field structure maps are judged to provide the more accurate information at a higher resolution than the Richardson (1966) map. Although the latter offers the appearance of complete coverage, its use could lead to significantly different and incorrect conclusions regarding the likelihood of a plume encountering a fault with a particular throw.

Accordingly, the strike and length of fault segments were measured from the structure map of each field. Segmentation of faults in this context was not purely topological as might be the case in other fault studies, which commonly place segment boundaries only at fault intersections or ends. Instead, segment

boundaries in this study were selected to capture the throw profile by recording this value at the ends of each segment. Segment boundaries were taken at the ends of faults (whether internal to the map or at its boundaries), at fault intersections, at most intersections of the fault with a structure contour, and at additional locations as needed. The latter were selected to provide segments along which the rate of change in throw along the fault is relatively constant. Figure 5 shows the fault segment boundaries selected on the structure map for one field. The sufficiency of the segment boundaries selected with regard to the purpose of this study is discussed in a following section.

The structural elevation at fault block corners was typically linearly projected, but in some cases, geologic judgment was used to adjust the resulting value to account for near-fault folding. Throws across faults at the block corners were calculated from these interpreted elevations. The structural elevation on the side of the fault opposite where a structure contour intersection was chosen as a segment boundary was generally linearly interpolated, and the throw was calculated. Figure 5 shows examples of fault block corner elevations and segment boundary throw estimates and shows that the throw along each segment typically varies.

Fault dip information was not given on the maps, so only the throw could be measured. As mentioned, most of the faults are understood to be vertical above the Vedder storage target and subvertical at the target, so measuring throw instead of dip displacement probably does not introduce significant errors. In addition, the faults have been identified as growth faults, so measuring throw should not generally introduce significant errors regarding the true displacement.

In addition, offset perpendicular to bedding is more related to shale-gouge ratio than is the actual displacement. The shale-gouge ratio is the proportion of shale displaced past a particular point on a fault. Fault permeability decreases with increasing shale-gouge ratio, at least at lower values (Yielding et al., 1996). Because the bedding dips in the vicinity of the pilot test site are generally small (7° for the Vedder Sand), the offset perpendicular to the bedding is almost the same as the throw, further justifying the use of throw in this study instead of true displacement.

The length and strike of 956 fault segments were measured. The total fault length measured was 465 km (289 mi). Throws were measured at 1046 points. The data are presented in Appendix 1 (AAPG Datashare 47, www.aapg.org/datashare).

Fault Strike

The distribution of fault strikes in fields centered off versus on the Bakersfield arch is shown on Figure 6. Off the arch, the primary and almost only strike mode is to the northwest. On the arch, the fault population exhibits this strike mode in addition to a north-striking mode and a lesser northeast-striking mode.

The distribution of fault strikes in fields centered on the shelf to upper slope versus the lower slope to deep basin is shown in Figure 7. Both populations show mostly the same modes in the same relative proportions, but the spread in the northwest and northeast modes is a bit greater in the lower shelf to basin population than the shelf to upper slope population.

A comparison of Figures 5 and 6 suggests that the main variation in fault strike pattern is off versus on the Bakersfield arch. The on-arch population appears to include the mode present in the off-arch population in addition to two other modes. This mode is parallel to the bedding strike as well as the basin margin and basin slope, which suggests that the mode may be caused by growth faulting. The second most common mode on the Bakersfield arch appears to be conjugate with the primary northern mode. This suggests that the secondary and tertiary modes at this location may be caused by the tectonic stresses that uplifted the Bakersfield arch.

As the pilot test site resides at the boundary of the Bakersfield arch, it is unclear from the above data which fault population strike modes to use in the analysis. In the course of investigating fault strike statistics, the strike distribution in oil and gas fields centered within 16 km (10 mi) of the pilot test site versus those farther away was plotted, as shown in Figure 8. Interestingly, the sole primary fault strike mode nearer the site is north to north-northwest. The reason for this is not clear, but given that the extent of the CO₂ sweep area from the pilot test

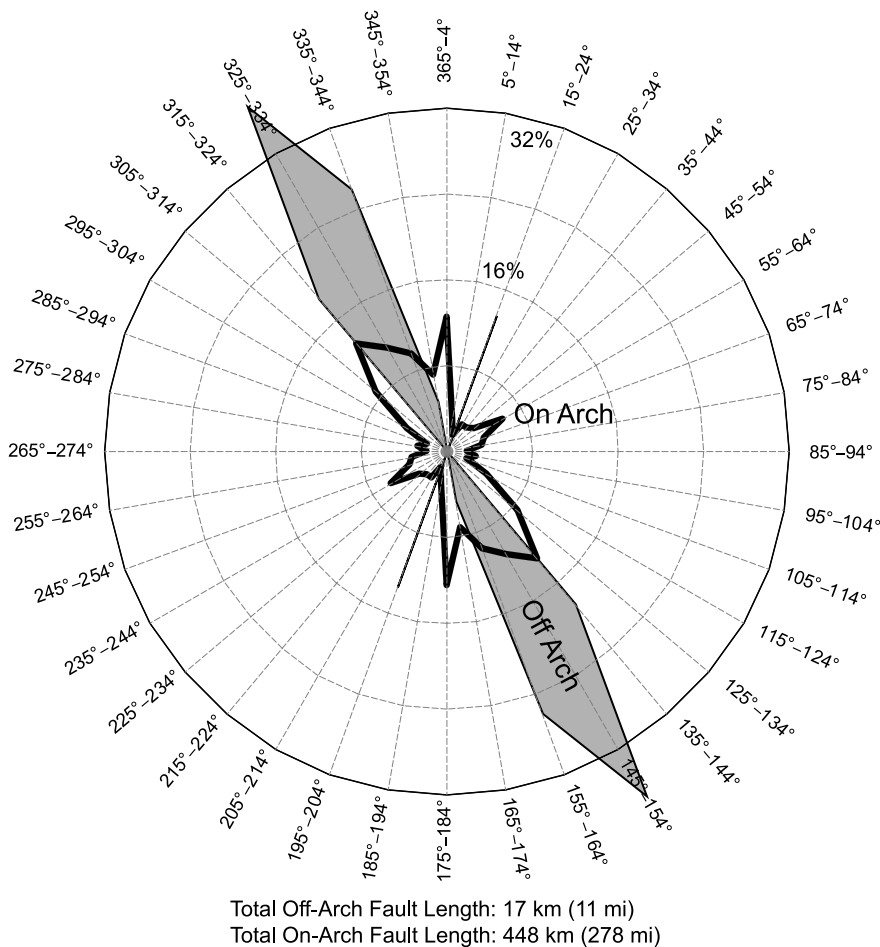


Figure 6. Percentage of fault length occurring in 10° strike intervals in oil and gas fields centered off versus on the Bakersfield arch in the vicinity of the pilot test site.

injection was anticipated to be much smaller than 16 km (10 mi), the one primary mode from the nearby fault population was selected for input to the plume-fault encounter probability calculation.

Throw Interpolation and Calculated Fault Density Robustness

The throw at one end of a fault segment will typically be different from that at the other end. Some methods for estimating the part of the segment with a particular d must be chosen. This method could be a linear interpolation between the displacements at the ends of the segment or some higher-order interpolation of displacement along the fault using multiple values. Alternatively, the segment length could simply be bifurcated with each half assigned to the throw from the nearer end. The simplicity of the latter strategy comes at the cost of error in F for a particular d given a specific fault, but this error

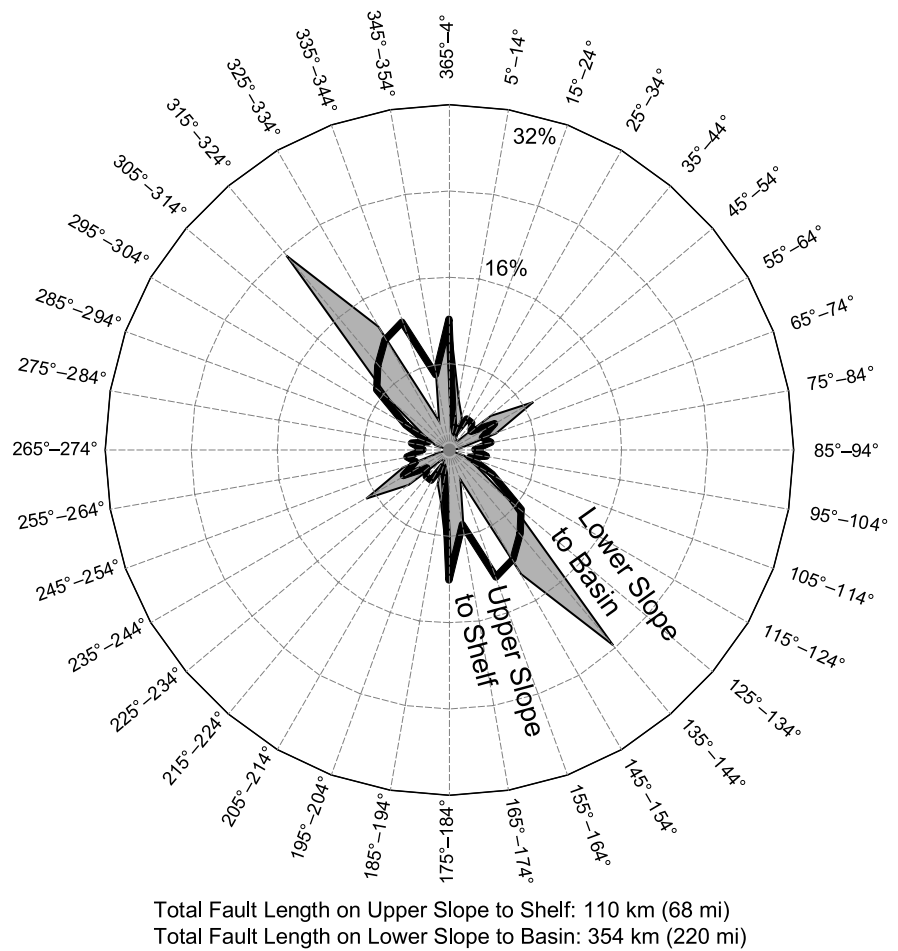
should shrink to a generally small value for a larger fault set.

In the case of the current set under consideration, F at different values of d was calculated using both the segment bifurcation and linear interpolation methods, as shown on Table 1. The difference in F at each d from these two methods was less than 5%, suggesting that the simpler bifurcation method can be used for larger fault sets.

The selection of fault segment boundaries could also affect the measured values of F . To test this, a decimated fault data set was created by deleting every other throw value along each fault and combining the segment length to either side into one segment. This resulted in a data set with 61% as many segments as the full data set.

The values of F from the decimated set using the linear interpolation method were less than 5% different than those from the full data set using linear interpolation, except for that at the highest value

Figure 7. Percentage of fault length occurring in 10° strike intervals in oil and gas fields centered on the upper slope to shelf versus the lower slope to basin in the vicinity of the pilot test site.



of d . At this d of 208 m (681 ft), F from the decimated set was still just 8% different than that from the full set.

The match of F from the decimated and full data sets indicates that the fault segments measured were more than sufficiently small to accurately capture the fault population statistics for the purposes of this study.

Vertical and Horizontal Fault Density Variation

The stratigraphic horizon on which the structure map for each field in California Division of Oil, Gas and Geothermal Resources (DOGGR) (1998) is constructed varies from field to field. Figure 4 shows that the faults in the vicinity of the pilot test tend to persist through the sub-Pliocene Tertiary section, which includes the Vedder Sand (California Division of Oil, Gas and Geothermal Resources [DOGGR], 1998). The fault density for each field is defined as

the total length of fault shown on the structure map for the field divided by the area of the map.

The vertical distances from the mapped horizon in each field to the Vedder Sand were measured from the geologic sections or stratigraphic columns available for each field (California Division of Oil, Gas and Geothermal Resources [DOGGR], 1998). Figure 9 shows the fault density from each structure map relative to the vertical distance from that horizon to the top of the Vedder.

The distribution of fault densities does not change appreciably within 1500-m (6900-ft) depth of the Vedder. Data beyond this are sparse but suggest that the density may be lower. Still, the figure supports aggregating the data from all the structure maps as reasonable with regard to varying horizons.

The other major consideration is whether data from the maps can be aggregated with regard to horizontal variation in the fault population. Although the major stratigraphic units are relatively continuous

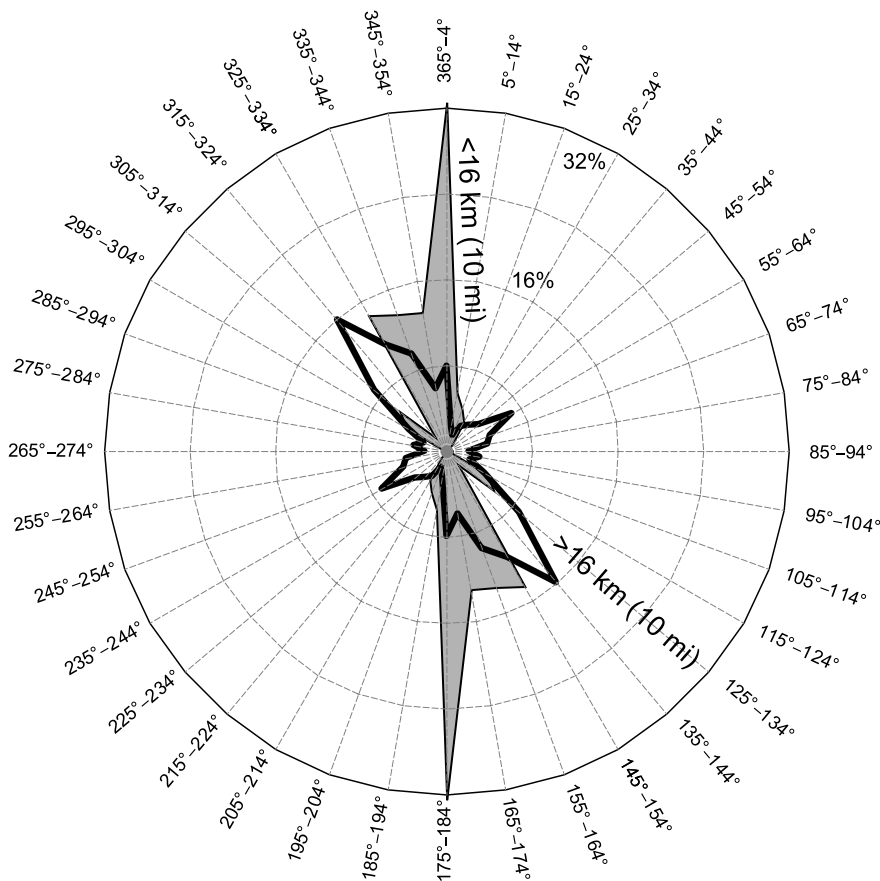


Figure 8. Percentage of fault length occurring in 10° strike intervals in oil and gas fields centered less versus more than 16 km (10 mi) from the pilot test site.

Total Fault Length in Fields Centered <16 km (10 mi) from Pilot Test Site: 81 km (50 mi)
 Total Fault Length in Fields Centered >16 km (10 mi) from Pilot Test Site: 384 km (239 mi)

across the area of data collection, as indicated in Figure 4, the site is located at the intersection of a depositional environment and a structural boundary as shown in Figure 3. The fault population could vary from one quadrant to another. For instance, there could be more growth faulting where the stratigraphic section is thicker, and/or more faulting over the Bakersfield arch.

Figure 10 shows the approximate direction and distance from the pilot test site to each field and the size of and the fault density in each. The figure shows almost no fields from the northwest to the northeast of the pilot test site. The fault density appears to be higher on the Bakersfield arch, whereas density does not seem to correlate to shelf versus basin. Unlike fault strike, no obvious trend in fault density with distance is observed. These data suggest that the pilot test site is in a transitional area between higher and lower fault densities because of its location at the margin of the Bakersfield arch.

To explore this further, fault density was computed for each quadrant bounded by the depositional and structural boundaries relative to the site shown in Figure 3. This density was calculated by dividing the sum of the fault segments by the sum of the structure map areas located in each quadrant. The data from Dyer Creek were assigned to the non-Bakersfield arch category based on the more recent work of Gautier and Scheirer (2007). Table 2 shows the results.

The three quadrants of off arch on shelf, on arch on shelf, and on arch in basin all have fault densities within approximately 35% of the average fault density. The largest quadrant density is approximately 80% higher than the smallest quadrant density. In contrast, the density in the off-arch basin quadrant is only approximately 10% of the average and 8% of the largest quadrant density.

However, the different quadrants have different average structure contour intervals. This, in turn,

Table 1. Fault Densities from the Full Data Set Via Different Methods and from the Decimated Set

Throw Truncation		Full Data Set					Decimated Data Set			
		Bifurcation		Linear Interpolation		Difference (%)	Linear Interpolation		Difference from Full Set Linear Interpolation Result (%)	
(m)	(ft)	(km/km ²)	(mi/mi ²)	(km/km ²)	(mi/mi ²)		(km/km ²)	(mi/mi ²)		
0.30	1.0	0.64	1.03	0.64	1.03	0.0	0.64	1.03	0.0	
0.46	1.5	0.64	1.03	0.64	1.03	0.0	0.64	1.03	0.0	
0.67	2.2	0.64	1.03	0.64	1.03	0.0	0.63	1.02	-1.6	
0.98	3.2	0.64	1.03	0.63	1.02	-1.6	0.63	1.02	0.0	
1.4	4.6	0.64	1.03	0.62	1.00	-3.1	0.62	1.00	0.0	
2.1	6.8	0.61	0.98	0.61	0.98	0.0	0.61	0.98	0.0	
3.0	10	0.58	0.94	0.58	0.94	0.0	0.58	0.94	0.0	
4.5	15	0.58	0.93	0.56	0.90	-3.4	0.56	0.90	0.0	
6.6	22	0.51	0.81	0.50	0.80	-2.0	0.50	0.81	0.0	
9.6	32	0.46	0.73	0.45	0.72	-2.2	0.45	0.72	0.0	
14	46	0.40	0.64	0.39	0.62	-2.5	0.39	0.62	0.0	
21	68	0.32	0.52	0.31	0.50	-3.1	0.31	0.50	0.0	
30	100	0.22	0.35	0.21	0.35	-4.5	0.21	0.34	0.0	
45	147	0.120	0.193	0.116	0.187	-3.3	0.113	0.182	-2.6	
66	215	0.076	0.122	0.073	0.117	-3.9	0.070	0.112	-4.1	
96	316	0.035	0.057	0.035	0.057	0.0	0.034	0.055	-2.9	
141	464	0.0089	0.0144	0.0093	0.0150	4.5	0.0089	0.0142	-4.3	
208	681	0.0025	0.0040	0.0025	0.0040	0.0	0.0023	0.0036	-8.0	

likely indicates different fault map resolution limits, with maps having smaller intervals likely to show faults with smaller throws than maps with larger intervals. All the areas have average contour intervals of approximately 30 m (100 ft) or less though, so the density of fault segments with throws greater than 30 m (100 ft) was also calculated and examined to reduce this confounding effect.

The density of these larger faults in the aforementioned group of three quadrants was again a reasonable match to the average fault density, although the variation from average increased to approximately 50% of the average, and the maximum variation between the quadrants grew to a factor of 2.

Fault Density Modeling

As indicated by Figures 2 and 9 as well as Table 2, the pilot test site is in a transitional location with regard to fault density. Experience at the Sleipner storage

project in the North Sea between Norway and the United Kingdom and the In Salah storage project in central Algeria indicates that it is difficult to simulate CO₂ migration direction and velocity even in hindsight, let alone predict it accurately (Chadwick et al., 2009; Durucan et al., 2011, respectively). The uncertainty in predicting CO₂ plume propagation direction demonstrated by the Sleipner and In Salah projects suggests that selecting the fault data from one or more of the geologic quadrants relative to the injection site could introduce larger errors in the analysis results than simply using the entire fault data set to develop average fault population statistics. The relative fault densities presented in Table 2 can be used to adjust the resulting probability up or down during injection depending on which direction the monitoring data indicate the plume is migrating.

Fault density from the entire data set is plotted against throw truncation (d_v) in Figure 11. Throw truncation is equivalent to the displacement cutoff for just the vertical component of offset. A throw

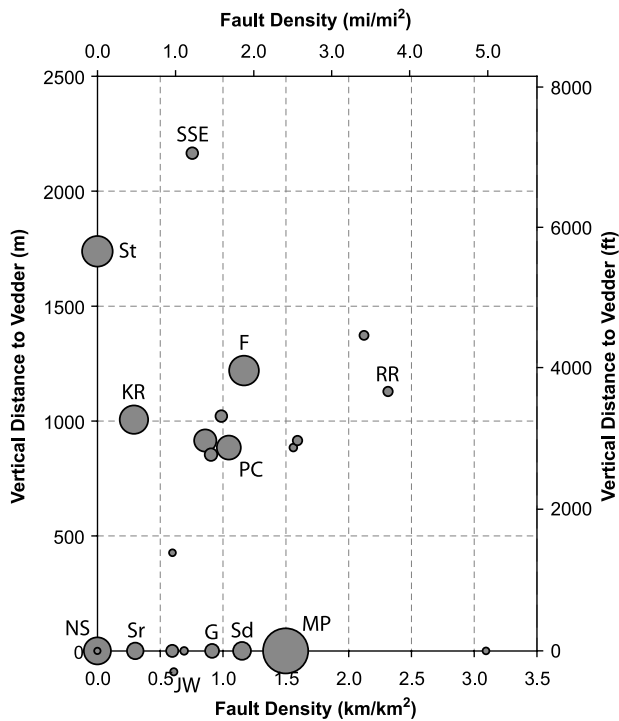


Figure 9. Fault density for individual oil and gas fields plotted against the vertical distance from the structural map horizon to the Vedder Sand. Positive values indicate that the Vedder is deeper than the map horizon. The symbol area is proportional to the field structure map area. Select data are labeled with field name initials. F = Fruitvale; G = Greeley; JW = West Jasmin; KR = Kern River; MP = Mount Poso; PC = Poso Creek; RR = Rosedale Ranch; St = Semitropic; Sr = Shafter; NS = North Shafter; SSE = Southeast Shafter; Sd = Strand. The location of each field is shown on Figure 3.

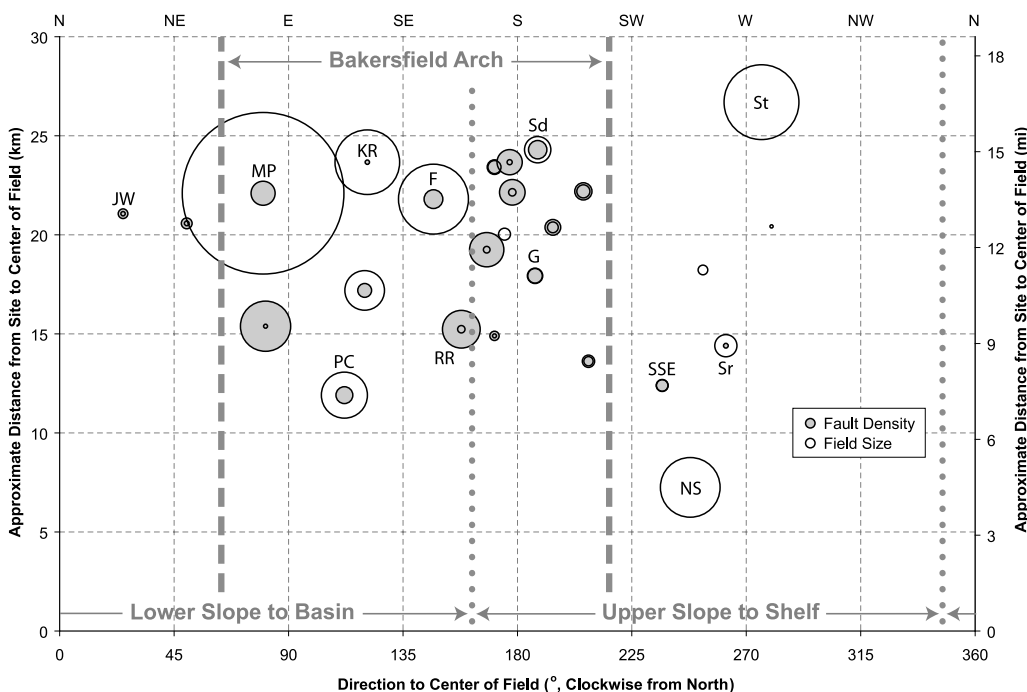


Figure 10. Approximate direction and distance to each field, with locations of depositional and structural boundaries indicated. Relative field structure map area and fault density are indicated by open and shaded circle sizes, respectively. Entirely unshaded circles are fields without faults. Select data are labeled with field name initials. F = Fruitvale; G = Greeley; JW = West Jasmin; KR = Kern River; MP = Mount Poso; PC = Poso Creek; RR = Rosedale Ranch; St = Semitropic; Sr = Shafter; NS = North Shafter; SSE = Southeast Shafter; Sd = Strand. The location of each field is shown on Figure 3.

truncation value refers to the parts of all faults with throws greater or equal to this value, whereas a displacement cutoff value refers to the parts of all faults with displacement, whether dip, strike, or oblique, greater than a certain value.

Although it is tempting to see the distribution in Figure 11 as exponential given the good fit to the data, low-displacement faults are underreported because of the fault mapping resolution limit (Pickering et al., 1995). The resolution limit is that throw below which the mapping method used and the data being used are unable to discriminate substantially all of the faults present within a map area. As a result, the actual fault population is larger than the measured population below the resolution limit. For instance, structure maps based on unit tops in well logs do not resolve all the faults seen in core samples. The latter allows the detection of faults with smaller offsets than the former. So, the exponential fit, as good as it is, actually underpredicts the fault density at low throw truncations.

Alternatively, the throw truncation intervals and range of values fitted were varied to find the largest range that could be well fit linearly. This resulted in a line that lies above the data at a low throw truncation, in accordance with the mapping resolution effect.

Table 2. Fault Density in the Vicinity of the Pilot Test Site

Depositional and Structural Area*	Total Field Area			Area-weighted Average Contour Interval (ft)	Fault Density			
	(km ²)	(mi ²)	(%)		All		≥100-ft Throw	
					(km/km ²)	(mi/mi ²)	(km/km ²)	(mi/mi ²)
All	550	210	100	94.6	0.84	1.36	0.24	0.38
Shelf	310	120	56	108.5	1.14	1.84	0.36	0.58
Basin	240	92	44	76.5	0.46	0.74	0.08	0.13
On arch	400	155	73	100.4	1.11	1.79	0.32	0.51
Off arch	148	57	27	78.7	0.112	0.180	0.0186	0.030
On arch (on shelf)	300	117	55	110	1.15	1.86	0.36	0.58
Off arch (on shelf)	7.5	2.9	1	50	0.68	1.10	0.18	0.29
On arch (in basin)	100	38	18	71.2	0.99	1.59	0.19	0.31
Off arch (in basin)	141	54	26	80.3	0.087	0.140	0.00	0.00

*Figure 3 shows the depositional and structural areas.

The point of departure of the linear fit from the fault density data is at a throw truncation of approximately 20 m (65 ft). The contour interval of most of the structure maps is 15 or 30 m (50 or 100 ft). The minimum interval is 6 m (20 ft), and the maximum is 61 m (200 ft). The contour interval average, standard deviation, kurtosis, and skewness are 23 m (76 ft), 14 m (48 ft), 1.85, and 1.21, respectively. This indicates that the distribution of contour intervals is relatively peaked at the average and symmetric at about the average. So, the point of departure between the fault density data and a linear fit matches the average structure contour interval.

Consequently, the linear fit more accurately represents the actual fault population in the vicinity of the pilot test site, indicating that the fault population follows a power-law distribution. The power-law fit also yields higher fault density estimates at low throw truncations, which makes it more conservative than the exponential fit for estimating leakage risk.

The linear fit also overpredicts the fault density at high throw truncations relative to the data according to Figure 11. This occurs because of the probability of undersampling of large faults in a given finite mapping area. This typically results in a greater downscaling in the throw truncation range than in the fault density range. This causes the data to shift

down at the highest throw truncations, the so-called “finite-range effect” of Pickering et al. (1995).

Pickering et al. (1995) presents a correction for this effect. The suggested correction was implemented by including the fault density at the two highest throw truncations in the data set for fitting, adding a constant to each fault density in the data set, and calculating a new linear fit. The constant was varied until the square of the correlation coefficient was maximized. A constant of 0.025 km/km² (0.04 mi/mi²) provided the best fit. The corrected data and fit are shown in Figure 12. The C_d resulting from this correction is 1.16.

A comparison of C_d values from Figures 10 and 11 provides additional support for taking the latter as more accurately representing the fault population than the former. The C_d of 1.43 shown in Figure 11 is larger than the values typically reported from field studies using scan lines, which range from 0.5 to 1.0 (Yielding et al., 1996). However, Marrett and Allmendinger (1991) discuss the shift in the value of the coefficient resulting from bias introduced by sampling in a dimensional space other than the space of interest. The parameter C_d in this article regards the fault population measured in a 2-D sampling space. Consequently, it is equivalent to C'_1 in Marrett and Allmendinger (1991). From a review of a previous work, Marrett and Allmendinger (1991) suggest the range of C'_1 is 1.0 to 1.7.

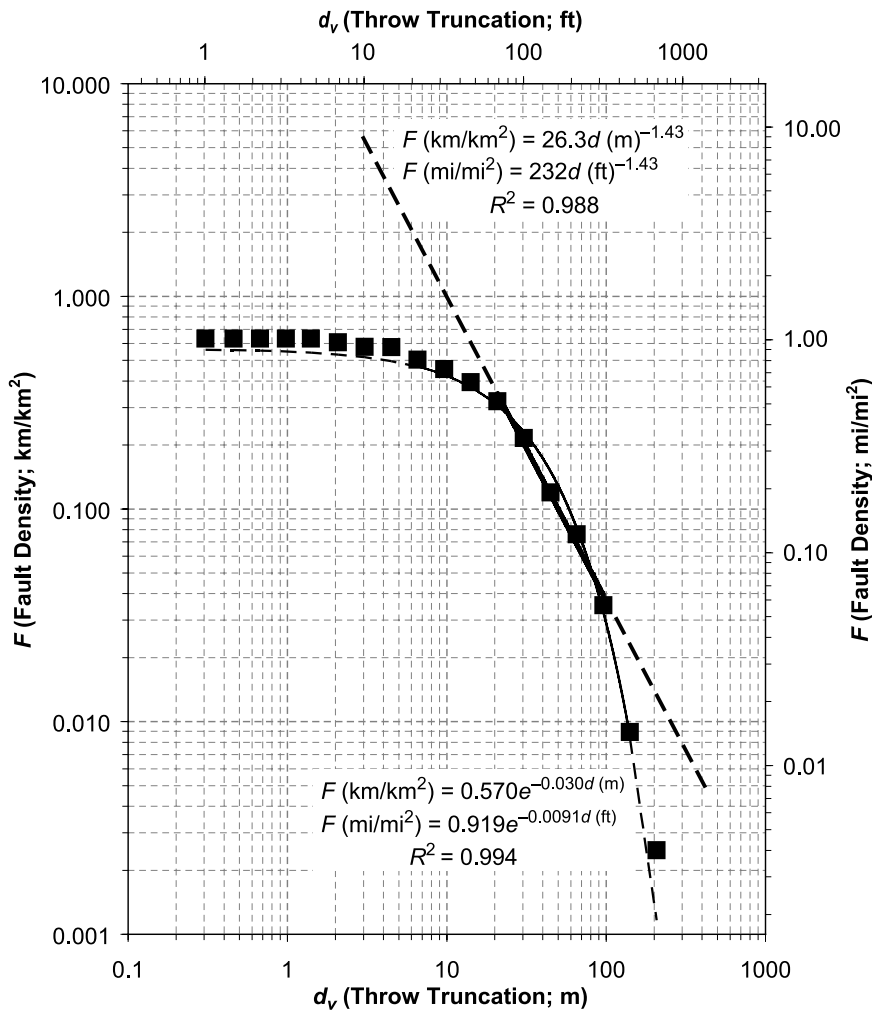


Figure 11. Fault density (F) versus throw truncation (d_v) aggregated from the structure maps for the oil and gas fields is shown in Figure 3. F is the areal density of the parts of all faults with a throw greater than d_v . Data are shown as closed boxes. The heavy line is a linear fit to selected data (see text). The lighter line is an exponential fit to all data. Dashed lines are extrapolated from the fit lines.

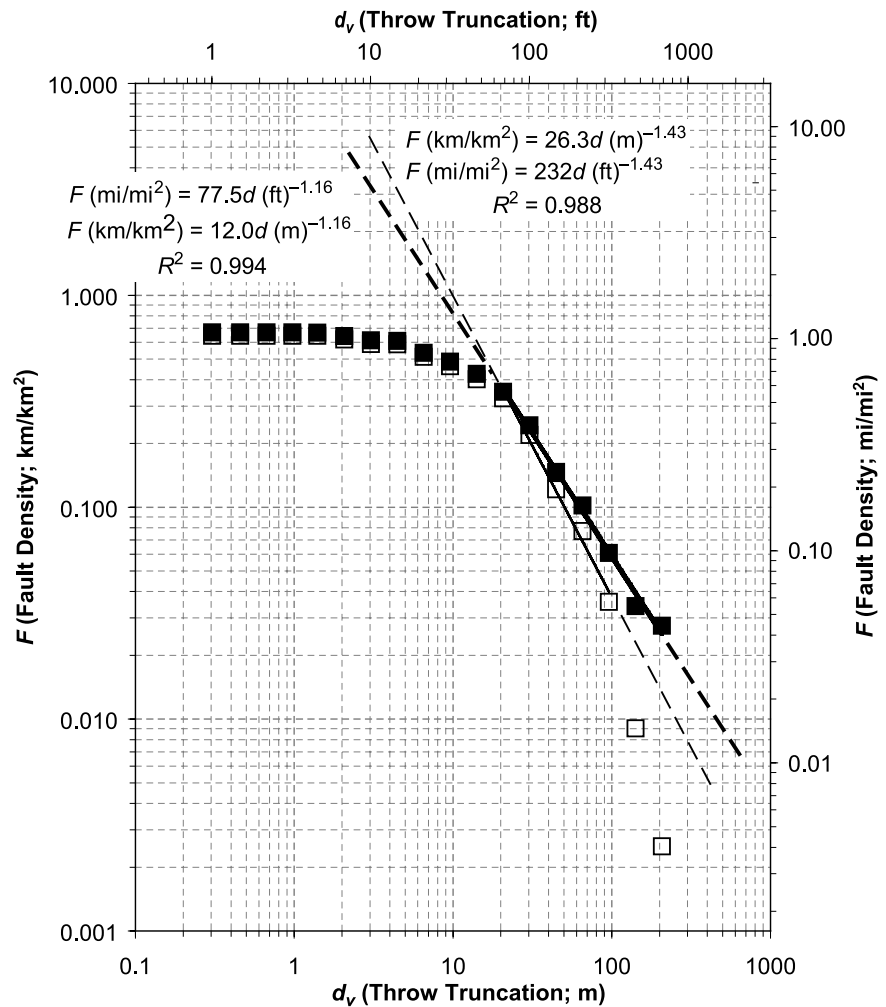
The 1.43 value of C_d shown in Figure 11 is within the range of 1.0 to 1.7. However, Cowie et al. (1995) found that the value of C_d declines as strain accumulates. This occurs because, as strain increases, an increasing proportion is taken up by greater displacement on existing faults as they link than by nucleation of new faults. This increases the proportion of larger faults relative to smaller faults in the population. The 1.43 value of C_d shown in Figure 11 is above the midpoint of the 1.0 to 1.7 range, suggesting that the fault network is still relatively undeveloped. However, most of the faults on the fault maps, such as those in Figure 5, intersect other faults, suggesting that the fault network is significantly developed. This would tend to support the contention that the C_d on Figure 11 is too large. The corrected C_d of 1.16 shown in Figure 12 is more commensurate with the observed degree of fault network development.

Fault Encounter Probability

An estimate of the reservoir area swept by CO_2 because of the proposed injection can be measured from numerical simulation results. The anticipated CO_2 plume at the pilot test site was numerically simulated using the ECO2N equation of the state package of TOUGH2 (Doughty, 2010). The model simulated the injection of 250,000 t/yr of CO_2 for 4 yr then simulated migration and trapping of the plume over the next 46 yr. Figure 13 shows CO_2 saturation (S_g) and saturation above residual saturation ($S_g - S_{gr}^A$) at several time steps in the numerical modeling. Saturation above residual is referred to as the “mobile fraction.” In Figure 13, a value of 0 indicates no saturation above residual, and a value of 1 indicates 100% saturation.

The area within the outer contour on the last frame of Figure 13 is taken as the region swept by

Figure 12. Areal fault density (F) versus throw truncation (d_v) aggregated from the structure maps for the oil and gas fields shown on Figure 3. Data are shown as open boxes. The lighter line is a linear fit to selected data (see text). Data corrected for the finite range effect using the approach of Pickering et al. (1995) are shown as closed boxes. The heavy line is a linear fit to selected corrected data. Dashed lines are extrapolated from the fit lines.



CO₂ since the start of injection. Little mobile CO₂ remaining at the plume front 20 yr after the start of injection is observed, so the area swept by CO₂ at this time is taken as the total sweep area for the purposes of analyzing the probability of mobile CO₂ encountering a fault.

Considering the predominant 170° fault strike mode in the vicinity of the pilot test site shown in Figure 8, the fault-perpendicular plume dimension, 2λ , is 1.40 km (0.87 mi) from Figure 13. Faults with throws that fully offset the cap rock overlying a prospective storage reservoir are one particular focus of concern (not that leakage along faults with smaller throws is not possible). The sealing formations over the Vedder have a vertical thickness of approximately 180 m (600 ft) (Wagoner, 2009). The corrected fault density equation on Figure 12 indicates that the average density of faults with this throw

truncation is 0.029 km/km² (0.047 mi/mi²). So, the probability of the plume resulting from the proposed pilot test injection encountering such a fault is 4.1% according to equation 8.

The numerical plume simulation did not account for any potential permeability anisotropy along bedding caused by faulting, although fault zones tend to have either higher or lower permeability than the host reservoir rock. Either case results in a higher permeability parallel to faults in the reservoir. As a first exploration of the effect of horizontal anisotropy, Doughty (2010) also simulated cases with an along-bedding anisotropy of 3 to 1 and 10 to 1 to the north. The dimensions of these sweep areas perpendicular to the predominant fault mode is 1.03 km (0.63 mi) and 0.76 km (0.47 mi), respectively. From equation 8, these result in probabilities of 3.0% and 2.2% for the plume encountering a fully seal offsetting fault. This

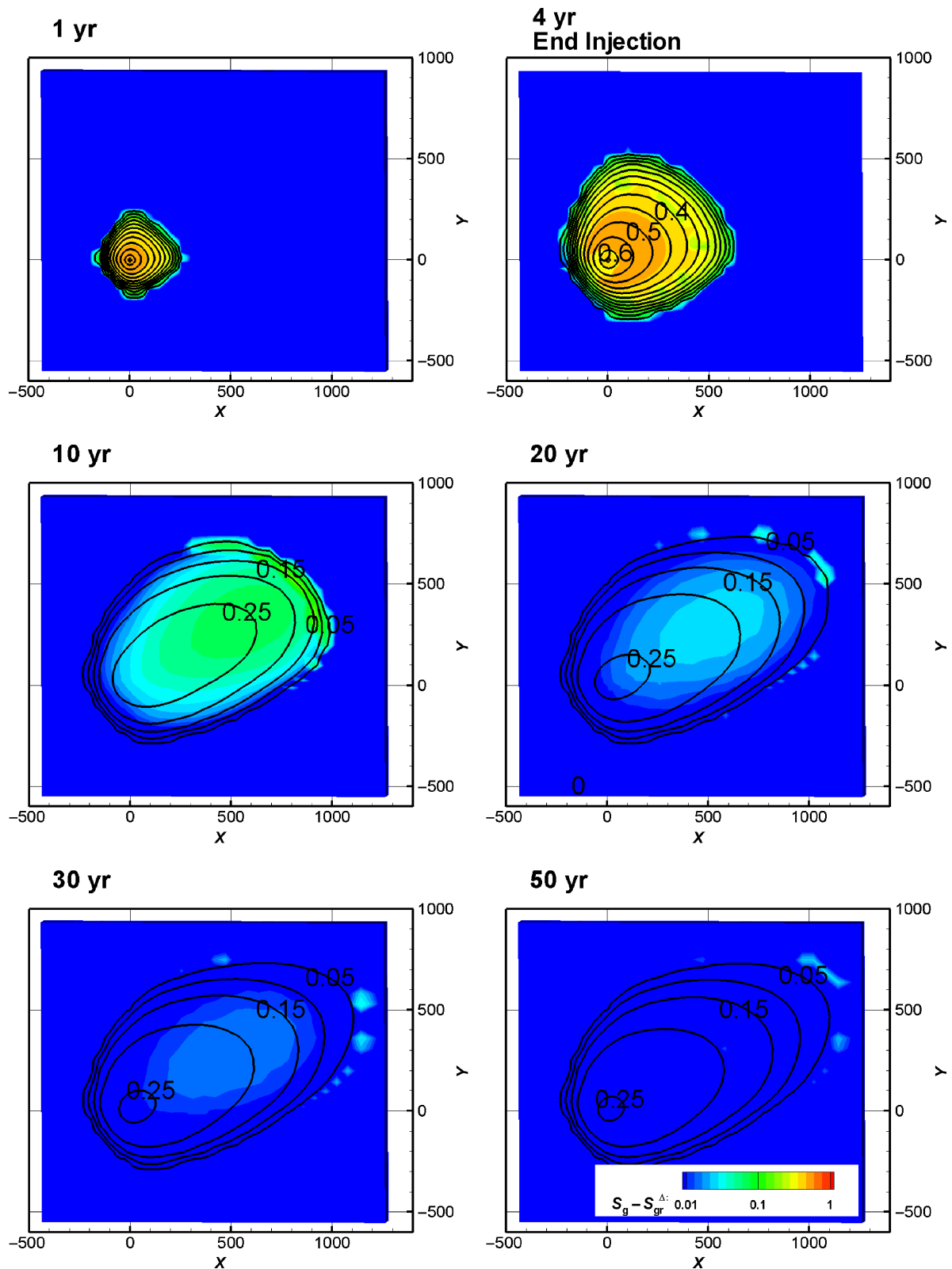


Figure 13. Map view of numerically simulated total carbon dioxide saturation (S_g) and saturation in excess of residual ($S_g - S_{gr}^{\Delta}$) resulting from the previously proposed pilot test (S_{gr} is the residual gas saturation). The Δ refers to the use of a hysteretic residual gas saturation function in the modeling. Total saturation is shown by contours. Saturation in excess of residual is shown by tints. Note that the tints for saturation in excess of residual are defined on a log scale. The axes are in meters. North is up. Courtesy of Christine Doughty, Lawrence Berkeley National Laboratory.

suggests that anisotropy caused by faults with small throws can reduce the probability of plumes encountering faults with large throws.

The density of faults with throws equal to half the seal thickness is 0.065 km/km^2 (0.10 mi/mi^2), so the probability of the plume encountering such a fault is 9%. This is offered not because a fault with this throw is particularly significant in terms of leakage consideration, but instead because shortly after the completion of this study, data became available, indicating that the Pond fault had a throw approximately half the seal thickness through the Vedder 2.8 km (1.7 mi) northeast of the prospective injection site (Wagoner, 2009).

The length of the simulated area swept by the plume toward the Pond fault is 1 km (0.62 mi). So, if the plume were approximately 2.8 times larger, it would encounter the Pond fault. This translates to a 25% encounter probability by equation 8. Note that the northwestern strike of the Pond fault falls in the small secondary strike mode containing 10% of the fault length in oil and gas fields centered within 16 km (10 mi) of the site, as shown in Figure 8.

The 25% encounter probability estimation is obviously considerably less than the actual unitary probability of encounter. However, it is sufficiently high to motivate consideration of such a fault encounter during the selection and design of a prospective carbon storage project, which, in turn, would hopefully motivate focused characterization efforts. Consequently, it appears that the method would have succeeded in this instance. Nonetheless, this single before and after outcome regarding the probability of a plume–Pond fault encounter provides only the beginning of testing the validity and use of the methodology presented in this article.

CONCLUSIONS

Storage of CO_2 in subsurface reservoirs is one possible means for reducing greenhouse gas emissions. However, the volume of depleted oil and gas fields is insufficient and is likely to be further limited by concerns regarding injecting CO_2 into the remaining resource in place. Consequently, if this technological

solution is to move forward, storage in brine-filled reservoirs will need to occur. Less is known about these reservoirs than those containing oil and gas because little economic incentive has existed to characterize them.

The possibility of leakage is one of the main concerns regarding CO_2 storage, with leakage along faults as a particular focus of concern. For leakage to occur along a fault, the CO_2 plume must encounter a fault, followed by CO_2 flow along the fault. The probability of the first step, fault encounter, can be calculated from statistics regarding fault orientation and areal fault density and from the numerical simulation of the CO_2 sweep area. This is particularly useful when conducting leakage risk assessment in the site-screening stage, or in the site-evaluation stage, at sites with limited site-specific characterization of faults.

Once the probability of a plume encountering a fault of a particular size is known, some perspective on the probability of leakage along that fault can be gained from its throw and the lithology of the displaced section by calculating the shale-gouge ratio along the fault (Yielding et al., 1996). The probability of a fault-plume encounter multiplied by the probability of fault leakage once an encounter has occurred comprises the total fault leakage probability. However, this presumes that fault encounter and leakage along a fault are independent events. Consequently, this approach would not hold in some cases, such as fields with a significant probability of fault reactivation on the faults of interest.

One outcome of the application of the fault population approach to fault encounter probability assessment is the realization that CO_2 plumes will encounter faults of some size in most geologic sequestration environments because small-offset faults occur at high densities. This does not mean a priori that significant leakage will necessarily occur via these smaller faults, as evidenced by the persistence of buoyant hydrocarbon deposits commonly, if not typically, occurring in association with faulted terrain. This understanding should shift the consideration of leakage via faults from a more simple concern for plumes encountering faults to a more detailed assessment of which faults are likely

to be of concern and what happens if the plume encounters those faults. For instance, although leakage may not occur, deflection of the plume relative to a homogeneous reservoir permeability assumption is likely caused by permeability alteration by faults.

REFERENCES CITED

- Ackermann, R. V., R. W. Schlische, and M. O. Withjack, 2001, The geometric and statistical evolution of normal fault systems: An experimental study of the effects of mechanical layer thickness on scaling laws: *Journal of Structural Geology*, v. 23, p. 1803–1819, doi:10.1016/S0191-8141(01)00028-1.
- Bartow, J. A., 1991, The Cenozoic evolution of the San Joaquin Valley, California: U.S. Geological Survey Professional Paper 1501, 40 p.
- Benson, S. M., and P. Cook, (coordinating authors), 2005, Underground geological storage, in P. Freund (coordinating author), Intergovernmental panel on climate change special report on carbon dioxide capture and storage: Cambridge, United Kingdom, Cambridge University Press, p. 195–276.
- Bloch, R. B., 1986, Ramp-style deposition of Oligocene marine Vedder Formation, San Joaquin Valley, California (abs.): *AAPG Bulletin*, v. 70, p. 463.
- California Division of Oil, Gas and Geothermal Resources (DOGGR), 1998, California oil and gas fields, volume I: Central California: Sacramento, California, California Division of Oil, Gas, and Geothermal Resources, 507 p.
- Callaway, D. C., 1990, Organization of stratigraphic nomenclature for the San Joaquin Basin, California, in J. G. Kuespert and S. A. Reid, eds., *Structure, stratigraphy, and hydrocarbon occurrences of the San Joaquin Basin, California*: Bakersfield, California: Pacific Sections of SEPM and AAPG, p. 5–21.
- Chadwick, R. A., D. Noy, R. Arts, and O. Eiken, 2009, Latest time-lapse seismic data from Sleipner yield new insights into CO₂ plume development, in J. Gale, H. Herzog, and J. Braitsch, eds., *Greenhouse gas control technologies 9: Proceedings of the 9th International Conference on Greenhouse Gas Control Technologies*, Washington, DC, November 16–20, 2008: *Energy Procedia*, v. 1, p. 2103–2110, doi:10.1016/j.egypro.2009.01.274.
- Cowie, P. A., D. Sornette, and C. Vanneste, 1995, Multifractal scaling properties of a growing fault population: *Geophysical Journal International*, v. 122, p. 457–469, doi:10.1111/j.1365-246X.1995.tb07007.x.
- Doughty, C., 2010, Investigation of CO₂ plume behavior for a large-scale pilot test of geologic carbon storage in a saline formation: *Transport in Porous Media*, v. 82, p. 49–76, doi:10.1007/s11242-009-9396-z.
- Durucan, S., J.-Q. Shi, C. Sinayuc, and A. Korre, 2011, In Salah CO₂ storage JIP: Carbon dioxide plume extension around KB-502 well—New insights into reservoir behavior at the In Salah storage site, in J. Gale, C. Hendriks, and W. Turkenberg, eds., *Greenhouse gas control technologies 10: Proceedings of the 10th International Conference on Greenhouse Gas Control Technologies*, Amsterdam, The Netherlands, November 16–20, 2008, *Energy Procedia*, v. 4, p. 3379–3385, doi:10.1016/j.egypro.2011.02.260.
- Energy Information Agency (EIA), 2009, Emissions of greenhouse gases report: <http://www.eia.doe.gov/oiaf/1605/ggprt/carbon.html> (accessed October 24, 2012).
- Gale, J. (coordinating author), 2005, Sources of CO₂, in P. Freund (coordinating author), Intergovernmental panel on climate change special report on carbon dioxide capture and storage: Cambridge, United Kingdom, Cambridge University Press, p. 75–103.
- Gautier, D. L., and A. H. Scheirer, 2007, Miocene total petroleum system: Southeast stable shelf assessment unit of the San Joaquin Basin province, in A. H. Scheirer, ed., *Petroleum systems and geologic assessment of oil and gas in the San Joaquin Basin province, California*: U.S. Geological Survey Professional Paper 1713, 19 p.
- Graham, S. A., and L. A. Williams, 1985, Tectonic, depositional, and diagenetic history of Monterey Formation (Miocene), central San Joaquin Basin, California: *AAPG Bulletin*, v. 69, p. 385–411.
- Hardacre, K. M., and P. A. Cowie, 2003, Controls on strain localization in a two-dimensional elastoplastic layer: Insights into size-frequency scaling of extensional fault populations: *Journal of Geophysical Research*, v. 108, no. B11, p. 2529, doi:10.1029/2001JB001712.
- Jordan, P. D., C. M. Oldenburg, and J. P. Nicot, 2011, Calculating the probability of injected carbon dioxide plumes encountering faults: *Greenhouse gases: Science and Technology*, v. 1, p. 160–174.
- Marrett, R., and R. Allmendinger, 1991, Estimates of strain due to brittle faulting: Sampling of fault populations: *Journal of Structural Geology*, v. 13, p. 735–738.
- McPherson, B. A., 1978, Sedimentation and trapping mechanisms in upper Miocene Stevens and older turbidite fans of the southeastern San Joaquin Valley, California: *AAPG Bulletin*, v. 62, p. 2243–2274.
- National Energy Technology Laboratory (NETL), 2009, West Coast Regional Sequestration Partnership: Development phase: <http://www.netl.doe.gov/publications/factsheets/project/Proj596.pdf> (accessed June 9, 2009).
- Pickering, G., J. M. Bull, and D. J. Anderson, 1995, Sampling power-law distributions: *Tectonophysics*, v. 248, p. 1–20, doi:10.1016/0040-1951(95)00030-Q.
- Richardson, E. E., 1966, Structure contours on top of the Vedder Sand, southeastern San Joaquin Valley, California: U.S. Geological Survey Open-File Report OF-66-110, 15 p.
- Scheirer, A. H., and L. B. Magoon, 2007, Age, distribution and stratigraphic relationship of rock units in the San Joaquin Basin Province, California, in A. H. Scheirer, ed., *Petroleum systems and geologic assessment of oil and gas in the San Joaquin Basin province, California*: U. S. Geological Survey Professional Paper 1713, 107 p.

- Wagoner, J., 2009, 3D Geologic modeling of the southern San Joaquin Basin for the Westcarb Kimberlina Demonstration Project—A status report: Livermore, California, Lawrence Livermore National Laboratory, 25 p.
- Watterson, J., J. J. Walsh, P. A. Gillespie, and S. Eaton, 1996, Scaling systematics of fault sizes on a large-scale range fault map: *Journal of Structural Geology*, v. 18, p. 199–214.
- Yielding, G., B. Freeman, and D. T. Needham, 1996, Quantitative fault seal prediction: *AAPG Bulletin*, v. 81, p. 897–917.
- Zhang, Y., C. M. Oldenburg, and S. Finsterle, 2010, Percolation-theory and fuzzy rule-based probability estimation of fault leakage at geologic carbon sequestration sites: *Environmental Earth Sciences*, v. 59, no. 7, p. 144–159, doi:10.1007/s12665-009-0131-4.

Datashare 47:

Measuring and modeling fault density for CO₂ storage plume-fault encounter probability estimation

Preston D. Jordan, Curtis M. Oldenburg, and Jean-Philippe Nicot

APPENDIX 1: FAULT POPULATION DATA

The following table presents fault data from select oil and gas field structure maps in California Division of Oil, Gas and Geothermal Resources (DOGGR) (1998). Fault segment boundaries were selected at the mapped ends of faults, fault intersections, and along faults as needed to capture the throw profile. The latter were commonly selected at the location where a structure contour intersected a fault.

“Start” and “end” under “throw” refer to the apparent throw at the first end of a fault segment encountered as measurement proceeded along a fault and the last end, respectively. Consequently, where segments connect along a fault, the apparent throw at the end of one segment will be the same as the apparent throw at the start of the next segment.

Field	Fault Number	Segment	Length (ft)	Strike (°Clockwise from North)	Throw at the Start of Segment (ft)	Throw at the End of Segment (ft)	Note
Bellevue	1	1	870	9	35	65	
Bellevue	1	2	1038	8	65	110	
Bellevue	1	3	732	6	110	165	
Bellevue	1	4	534	8	165	240	
Bellevue	1	5	656	6	240	295	
Bellevue	1	6	824	10	295	345	
Bellevue	1	7	778	8	345	380	
Bellevue	1	8	763	8	380	395	
Bellevue	1	9	763	9	395	330	
Bellevue	1	10	961	9	330	270	
Bellevue	1	11	1083	4	330	320	
Bellevue	1	12	1190	4	320	255	
Bellevue	1	13	870	0	255	165	
Bellevue	1	14	4059	179	165	125	
Bellevue	2	1	748	132	20	20	
Bellevue	2	2	2243	123	20	30	
Bellevue	2	3	626	123	30	75	
Bellevue	2	4	794	117	75	75	
Bellevue	2	5	977	114	75	60	
Bellevue	2	6	977	115	60	75	
Bellevue	2	7	687	108	75	60	
Bellevue	3	1	1862	140	10	40	
Bellevue	3	2	1877	139	40	45	
Bellevue	3	3	2960	141	45	45	
Bellevue	3	4	1801	140	45	15	
Bellevue West	1	1	2071	142			
Bellevue West	1	2	975	143			
Bellevue West	2	1	457	122	5	5	
Bellevue West	2	2	802	120	5	10	
Bellevue West	2	3	630	117	10	5	
Bellevue West	2	4	640	118	5	10	
Bellevue West	2	5	538	112	10	10	
Bellevue West	2	6	518	110	10	10	
Bellevue West	3	1	711	134	15	15	
Bellevue West	3	2	995	134	15	5	
Bellevue West	3	3	670	133	5	5	
Bellevue West	3	4	721	133	10	15	
Bellevue West	3	5	589	131	15	15	
Bellevue West	3	6	335	133	15	10	
Bellevue West	3	7	294	133	45	30	
Bellevue West	3	8	447	131	30	25	
Bellevue West	3	9	447	129	25	25	
Bellevue West	3	10	284	131	25	20	
Bellevue West	4	1	1472	70	20	15	
Bellevue West	4	2	762	68	15	10	
Bellevue West	4	3	741	70	10	15	
Bellevue West	4	4	914	68	15	10	
Bellevue West	4	5	599	67	25	20	

Field	Fault Number	Segment	Length (ft)	Strike (°Clockwise from North)	Throw at the Start of Segment (ft)	Throw at the End of Segment (ft)	Note
Bellevue West	4	6	883	67	85	65	
Bellevue West	4	7	1432	64	65	0	
Bellevue West	4	8	843	61	0	25	
Bellevue West	4	9	853	58	25	35	
Bellevue West	5	1	274	47	15	15	
Bellevue West	5	2	467	49	15	10	
Bellevue West	5	3	538	46	10	15	
Bellevue West	5	4	467	44	15	15	
Bellevue West	5	5	650	40	15	30	
Bellevue West	5	6	437	38	30	0	
Bellevue West	5	7	437	38	0	30	
Bellevue West	5	8	619	36	30		
Bellevue West	5	9	416	33			
Bellevue West	6	1	1371	141	35	60	
Bellevue West	6	2	762	143	60	75	
Bellevue West	6	3	640	141	75	15	
Bellevue West	7	1	1310	140	65	40	
Bellevue West	7	2	1706	140	40	15	
Bellevue West	7	3	213	140	30	30	
Calders Corner	1	1	3727	136			
Calders Corner	1	2	2065	134	270	205	
Calders Corner	1	3	2034	124	205	100	
Calders Corner	1	4	714	121	100	65	
Calders Corner	1	5	2423	114			
Calders Corner	2	1	3339	142			
Calders Corner	2	2	1600	142	355	365	
Calders Corner	2	3	699	142	365	365	
Calders Corner	2	4	1227	139	365	385	
Calders Corner	2	5	1072	140	385	390	
Calders Corner	2	6	901	141			
Calders Corner	3	1	1211	60	40	45	
Calders Corner	3	2	1367	56	45	45	
Calders Corner	3	3	2019	55	45	180	
Calders Corner	4	1	1103	61			
Calders Corner	4	2	2485	55			
Dyer Creek	1	1	9141	143	155	155	
Fruitvale	1	1	3400	155			
Fruitvale	1	2	680	166			
Fruitvale	1	3	3360	164	35	15	
Fruitvale	1	4	560	170	10	10	
Fruitvale	1	5	480	169	45	25	
Fruitvale	1	6	3000	168	30	40	
Fruitvale	2	1	2240	147			
Fruitvale	2	2	1360	146			
Fruitvale	3	1	1520	151	90	90	
Fruitvale	3	2	3440	145	95	85	
Fruitvale	4	1	3680	147	95	60	
Fruitvale	5	1	1240	108	55	50	

Field	Fault Number	Segment	Length (ft)	Strike (°Clockwise from North)	Throw at the Start of Segment (ft)	Throw at the End of Segment (ft)	Note
Fruitvale	5	2	3040	110	50	35	
Fruitvale	6	1	6160	143	50	35	
Fruitvale	7	1	3560	123	0	55	
Fruitvale	7	2	1960	130	40	45	
Fruitvale	7	3	1800	130	10	0	
Fruitvale	7	4	4480	132	0	5	
Fruitvale	7	5	1080	132	5	5	
Fruitvale	7	6	2960	134	20	20	
Fruitvale	7	7	1840	141	20	20	
Fruitvale	7	8	1880	155	20	20	
Fruitvale	8	1	2560	134	35	15	
Fruitvale	8	2	4280	134	30	30	
Fruitvale	8	3	5320	134	30	0	
Fruitvale	9	1	1680	164			
Fruitvale	9	2	2840	164	0	0	
Fruitvale	9	3	2520	164	0	5	
Fruitvale	9	4	2280	163	5	10	
Fruitvale	9	5	2120	162	10	0	
Fruitvale	9	6	3400	162	0	0	
Fruitvale	9	7	2840	162	0	0	
Fruitvale	10	1	4360	96	10	10	
Fruitvale	11	1	1040	76			
Fruitvale	12	1	2320	89			
Fruitvale	12	2	1760	86			
Fruitvale	12	3	480	87			
Fruitvale	12	4	960	83			
Fruitvale	13	1	3720	77			
Fruitvale	14	1	640	73	35	35	
Fruitvale	14	2	1160	73	35	40	
Fruitvale	14	3	1000	73	40	30	
Fruitvale	14	4	1240	73	30	35	
Fruitvale	14	5	880	73	35	25	
Fruitvale	15	1	920	70	35	35	
Fruitvale	15	2	1920	72	120	40	
Fruitvale	15	3	2880	71	40	5	
Fruitvale	16	1	680	70	115	115	
Fruitvale	16	2	1440	63	0	15	
Fruitvale	16	3	1360	65	50	40	
Fruitvale	16	4	1400	64	35	35	
Fruitvale	16	5	1480	64	35	25	
Fruitvale	16	6	1400	64	25	5	
Fruitvale	16	7	1160	65	5	0	
Fruitvale	17	1	3000	55			
Fruitvale	17	2	1600	56	45	50	
Fruitvale	17	3	920	53	50	55	
Fruitvale	17	4	1160	64	15	15	
Fruitvale	17	5	1600	64	35	25	
Fruitvale	17	6	800	58	25	20	

Field	Fault Number	Segment	Length (ft)	Strike (°Clockwise from North)	Throw at the Start of Segment (ft)	Throw at the End of Segment (ft)	Note
Fruitvale	17	7	1120	60	60	55	
Fruitvale	17	8	1360	60	55	30	
Fruitvale	17	9	1400	58	30	5	
Fruitvale	17	10	1040	59	40	55	
Fruitvale	18	1	3840	58	15	0	
Fruitvale	18	2	2200	60	0	20	
Fruitvale	18	3	1120	60	20	25	
Fruitvale	18	4	1200	63	25	0	
Fruitvale	18	5	1000	65	0	10	
Fruitvale	19	1	2840	54			
Fruitvale	19	2	1600	54	55	55	
Fruitvale	19	3	840	54	55	50	
Fruitvale	19	4	960	54	50	50	
Fruitvale	19	5	920	54	50	80	
Fruitvale	19	6	1120	55	45	55	
Fruitvale	19	7	1640	54	55	60	
Fruitvale	19	8	1240	53	60	50	
Fruitvale	19	9	720	55	50	40	
Fruitvale	19	10	960	53	40	0	
Fruitvale	20	1	3240	72			
Fruitvale	20	2	1280	72	135	100	
Fruitvale	20	3	1240	73	100	60	
Fruitvale	20	4	1560	72	60	15	
Fruitvale	20	5	1280	73	15	0	
Fruitvale	20	6	1000	70	0	0	
Fruitvale	21	1	920	41	0	5	
Fruitvale	21	2	1200	40	5	0	
Fruitvale	21	3	1000	39	0	0	
Fruitvale	22	1	1200	0			
Fruitvale	22	2	2080	3	35	35	
Fruitvale	22	4	1400	2	35	5	
Fruitvale	22	5	1160	3	5	0	
Fruitvale	22	6	560	3	0	0	
Fruitvale	23	1	480	38	0	45	
Fruitvale	23	2	1240	35	45	65	
Fruitvale	23	3	2560	36	65	20	
Fruitvale	23	4	2200	35			
Fruitvale	24	1	160	30	0	5	
Fruitvale	24	2	960	30	5	20	
Fruitvale	24	3	1040	30	20	35	
Fruitvale	24	4	1280	31	35	70	
Fruitvale	25	1	2480	10			
Fruitvale	25	2	1040	8	235	250	
Fruitvale	25	3	2720	0	125	110	
Fruitvale	25	4	1760	0	180	120	
Fruitvale	25	5	1280	0	120	105	
Fruitvale	25	6	2160	0	105	85	
Fruitvale	25	7	3120	0	65	10	

Field	Fault Number	Segment	Length (ft)	Strike (°Clockwise from North)	Throw at the Start of Segment (ft)	Throw at the End of Segment (ft)	Note
Fruitvale	25	8	2080	169	0	0	
Fruitvale	26	1	1440	24	125	85	
Fruitvale	26	2	1480	28	855	120	
Fruitvale	26	3	1360	27	120	165	
Fruitvale	26	4	1920	28			
Goosloo	1	1	6065	140			
Goosloo	1	2	1542	136	145	105	
Goosloo	1	3	1897	137	105	135	
Goosloo	1	4	1042	136	135	150	
Goosloo	1	5	1230	134	50	90	
Goosloo	1	6	1938	133	90	140	
Goosloo	1	7	2147	137	140	175	
Goosloo	1	8	1167	141			
Goosloo	1	9	2960	164			
Goosloo	2	1	1459	129			
Goosloo	2	2	1396	127			
Goosloo	2	3	1897	125	40	20	
Goosloo	2	4	2605	125	60	30	
Goosloo	2	5	2814	128	0	15	
Goosloo	2	6	1605	131	25	20	
Goosloo	2	7	1459	135			
Goosloo	3	1	2647	25	40	100	
Greeley	1	1	4284	146			Right lateral
Greeley	1	2	1419	148	80	130	Right lateral
Greeley	1	3	928	144	130	90	Right lateral
Greeley	1	4	682	145	90	70	Right lateral
Greeley	1	5	2756	144	70	50	Right lateral
Greeley	1	6	1555	143	50	40	Right lateral
Greeley	1	7	3465	143	40	100	Right lateral
Greeley	1	8	12061	143			Right lateral
Greeley	2	1	3274	24			
Greeley	2	2	2565	14			
Greeley	2	3	2838	3			
Jasmin West	1	1	1200	162			
Jasmin West	1	2	1706	162	75	80	
Jasmin West	1	3	1020	162	80	70	
Jasmin West	1	4	1191	162	70	65	
Jasmin West	1	5	1309	162	65	70	
Jasmin West	1	6	614	162			
Kern Front	1	1	4718	133			
Kern Front	1	2	1377	141			
Kern Front	1	3	1722	153			
Kern Front	1	4	3030	164			
Kern Front	1	5	3857	176			
Kern Front	1	6	5751	1			
Kern Front	1	7	2720	14	95	70	
Kern Front	1	8	1240	29	70	50	
Kern Front	1	9	1240	28	50	20	

Field	Fault Number	Segment	Length (ft)	Strike (°Clockwise from North)	Throw at the Start of Segment (ft)	Throw at the End of Segment (ft)	Note
Kern Front	1	10	1894	39	20	0	
Kern Front	2	1	895	32	0	10	
Kern Front	2	2	1377	37	10	20	
Kern Front	2	3	2101	43	20	30	
Kern Front	3	1	2824	3			
Kern Front	3	2	2789	179	40	10	
Kern Front	3	3	2204	172	10	30	
Kern Front	3	4	1791	159	30	0	
Kern Front	4	1	826	59	0	25	
Kern Front	4	2	689	60	25	0	
Kern Front	5	1	2169	31			
Kern Front	5	2	1653	28	30	0	
Kern Front	5	3	2307	20	0	30	
Kern Front	5	4	1377	34	30	40	
Kern Front	5	5	1722	27	40	20	
Kern Front	5	6	895	19	20	0	
Kern Front	6	1	2479	43			
Kern Front	6	2	1756	52	85	120	
Kern Front	6	3	1102	36	120	120	
Kern Front	6	4	1756	26	120	70	
Kern Front	6	5	2893	28	70	20	
Kern Front	6	6	1963	48	20	0	
Kern Front	7	1	1997	50	0	5	
Kern Front	7	2	1515	42	5	5	
Kern Front	7	3	1653	43	5	5	
Kern Front	7	4	1240	51	5	0	
Kern Front	8	1	2238	29			
Kern Front	8	2	4201	20			
Kern Front	8	3	2169	8			
Kern Front	8	4	2101	176			
Kern Front	8	5	1756	165			
Kern Front	8	6	2101	157			
Kern River	1	1	3174	170			
Kern River	1	2	2527	175			
Kern River	1	3	2106	89			
Kern River	1	4	1684	7			
Kern River	1	5	1846	20			
Kern River	2	1	1749	138			
Kern River	2	2	2462	144			
Kern River	3	1	1846	136			
Kern River	3	2	2106	137			
Kern River	4	1	3401	70	100	85	
Kern River	4	2	4470	74			
Kern River	5	1	2235	104			China fault zone
Kern River	5	2	3920	100			China fault zone
Kern River	5	3	1814	97			China fault zone
Kern River	5	4	2494	91	60	100	China fault zone
Kern River	5	5	2786	94	100	135	China fault zone

Field	Fault Number	Segment	Length (ft)	Strike (°Clockwise from North)	Throw at the Start of Segment (ft)	Throw at the End of Segment (ft)	Note
Kern River	5	6	2073	95	135	160	China fault zone
Kern River	5	7	2235	99	60	40	China fault zone
Kern River	5	8	2235	103			China fault zone
McClung	1	1	2335	69			
McClung	2	1	719	140	40	15	
McClung	2	2	609	140	15	60	
McClung	2	3	770	140	60	70	
McClung	2	4	1117	141	70	5	
McClung	2	5	1312	140	15	20	
McClung	2	6	1532	141	20	20	
McClung	2	7	1591	140	20	20	
McClung	3	1	1100	141	80	45	
McClung	3	2	1650	140	45	65	
McClung	3	3	85	140	80	80	
McClung	3	4	618	141	45	25	
McClung	3	5	643	140	25	15	
McClung	3	6	1159	140	15	15	
McClung	3	7	1134	139	15	15	
McClung	3	8	1345	140	15	30	
McClung	4	1	626	59	10	45	
McClung	5	1	762	47	15	10	
McClung	5	2	542	45	10	15	
McClung	5	3	1168	43	15	20	
McClung	5	4	440	40			
Mount Poso	1	1	2459	144	130	130	
Mount Poso	1	2	2317	147	130	130	
Mount Poso	1	3	2128	149	80	75	
Mount Poso	1	4	2932	150	75	65	
Mount Poso	2	1	2317	97	20	20	
Mount Poso	2	2	1560	106	20	10	
Mount Poso	2	3	1702	115	10	5	
Mount Poso	2	4	1749	124	5	25	
Mount Poso	2	5	1277	127	25	30	
Mount Poso	2	6	1324	132	30	40	
Mount Poso	3	1	2033	141	80	80	
Mount Poso	3	2	1277	144	80	75	
Mount Poso	3	3	2459	145	65	75	
Mount Poso	3	4	1608	145	125	100	
Mount Poso	3	5	4303	146	125	140	
Mount Poso	3	6	2080	162	220	205	
Mount Poso	3	7	567	167	240	240	
Mount Poso	3	8	662	168	250	250	
Mount Poso	3	9	993	4	265	230	
Mount Poso	3	10	2411	166	230	170	
Mount Poso	3	11	1135	152	170	140	
Mount Poso	3	12	2695	118	220	240	
Mount Poso	3	13	993	164	410	410	
Mount Poso	3	14	993	175	410	405	

Field	Fault Number	Segment	Length (ft)	Strike (°Clockwise from North)	Throw at the Start of Segment (ft)	Throw at the End of Segment (ft)	Note
Mount Poso	3	15	3121	156	405	400	
Mount Poso	3	16	1749	143	400	405	
Mount Poso	3	17	1371	156	405	405	
Mount Poso	3	18	1135	168	405	410	
Mount Poso	3	19	1513	175	410	415	
Mount Poso	3	20	615	160	415	415	
Mount Poso	3	21	1040	135	120	110	
Mount Poso	3	22	662	131	110	105	
Mount Poso	3	23	3073	147	85	75	
Mount Poso	3	24	1939	148	75	80	
Mount Poso	3	25	5012	141	80	95	
Mount Poso	3	26	1749	139	95	95	
Mount Poso	3	27	2080	136	50	65	
Mount Poso	3	28	804	126	65	70	
Mount Poso	4	1	2553	126	55	55	
Mount Poso	4	2	1844	127	55	45	
Mount Poso	4	3	2742	127	15	75	
Mount Poso	4	4	1324	130	75	65	
Mount Poso	4	5	1608	133	55	35	
Mount Poso	4	6	1844	153	35	20	
Mount Poso	4	7	1040	134	20	10	
Mount Poso	4	8	1939	133	10	10	
Mount Poso	4	9	1277	129	20	5	
Mount Poso	4	10	2175	130	5	0	
Mount Poso	5	1	4208	179	60	60	
Mount Poso	6	1	2695	136	105	95	
Mount Poso	6	2	3499	136	120	105	
Mount Poso	7	1	1324	175	10	10	
Mount Poso	7	2	2222	179	195	215	
Mount Poso	8	1	1844	117	50	50	
Mount Poso	8	2	1371	110	50	40	
Mount Poso	8	3	1040	111	40	25	
Mount Poso	8	4	1182	119	25	5	
Mount Poso	8	5	1088	129	85	20	
Mount Poso	8	6	1797	144	20	20	
Mount Poso	8	7	1371	104	20	30	
Mount Poso	9	1	3357	157	90	40	
Mount Poso	9	2	473	154	50	50	
Mount Poso	9	3	1135	160	15	15	
Mount Poso	9	4	473	158	30	30	
Mount Poso	10	1	4114	0	45	70	
Mount Poso	10	2	1749	0	100	80	
Mount Poso	11	1	2837	117	70	100	
Mount Poso	12	1	1939	114	140	135	
Mount Poso	12	2	1466	114	50	65	
Mount Poso	12	3	1702	116	65	70	
Mount Poso	12	4	1891	116	70	80	
Mount Poso	13	1	615	163	15	20	

Field	Fault Number	Segment	Length (ft)	Strike (°Clockwise from North)	Throw at the Start of Segment (ft)	Throw at the End of Segment (ft)	Note
Mount Poso	13	2	1844	157	90	115	
Mount Poso	13	3	662	147	115	125	
Mount Poso	13	4	993	130	125	150	
Mount Poso	13	5	615	136	150	160	
Mount Poso	13	6	804	153	160	170	
Mount Poso	14	1	1277	108	70	90	
Mount Poso	14	2	1608	122	90	95	
Mount Poso	14	3	1088	131	95	95	
Mount Poso	14	4	1560	145	95	90	
Mount Poso	14	5	1324	155	90	100	
Mount Poso	14	6	1466	162	100	110	
Mount Poso	14	7	3877	168	110	140	
Mount Poso	14	8	1797	163	140	155	
Mount Poso	14	9	1277	157	155	165	
Mount Poso	14	10	3263	155	165	150	
Mount Poso	14	11	851	152	150	145	
Mount Poso	14	12	1891	141	145	130	
Mount Poso	14	13	2932	135	130	170	
Mount Poso	14	14	2884	140	170	165	
Mount Poso	14	15	1182	146	165	165	
Mount Poso	14	16	2175	148	165	140	
Mount Poso	14	17	3594	155	140	105	
Mount Poso	14	18	898	156	35	30	
Mount Poso	14	19	2459	158	40	45	
Mount Poso	14	20	3546	162	45	55	
Mount Poso	15	1	1277	113	130	100	
Mount Poso	15	2	1891	120	100	85	
Mount Poso	15	3	2128	126	85	95	
Mount Poso	16	1	2742	157	50	55	
Mount Poso	16	2	993	147	40	20	
Mount Poso	16	3	2270	144	175	150	
Mount Poso	16	4	4114	145	125	85	
Mount Poso	16	5	3263	146	85	75	
Mount Poso	16	6	2175	148	75	65	
Mount Poso	16	7	4870	152	65	110	
Mount Poso	16	8	5059	151	110	130	
Mount Poso	16	9	4587	152	130	150	
Mount Poso	16	10	4681	152	150	175	
Mount Poso	16	11	1702	153			
Mount Poso	16	12	2506	158			
Mount Poso	17	1	1939	117	155	130	
Mount Poso	17	2	1608	133	130	70	
Mount Poso	17	3	3215	147	70	50	
Mount Poso	17	4	2080	136	50	65	
Mount Poso	17	5	2175	131	65	120	
Mount Poso	17	6	946	131	120	130	
Mount Poso	18	1	2884	145	0	10	
Mount Poso	18	2	2932	145	10	0	

Field	Fault Number	Segment	Length (ft)	Strike (°Clockwise from North)	Throw at the Start of Segment (ft)	Throw at the End of Segment (ft)	Note
Mount Poso	18	3	804	150	0	15	
Mount Poso	18	4	1891	154	15	45	
Mount Poso	18	5	1088	146	45	65	
Mount Poso	18	6	946	138	65	90	
Mount Poso	18	7	1324	135	90	120	
Mount Poso	18	8	1419	142	120	130	
Mount Poso	18	9	1419	148	0	0	
Mount Poso	19	1	615	0	55	50	
Mount Poso	19	2	1277	0	50	40	
Mount Poso	20	1	4303	148	0	35	
Mount Poso	20	2	2222	152	35	40	
Mount Poso	20	3	1419	140	40	40	
Mount Poso	20	4	1371	133	40	55	
Mount Poso	20	5	2033	124	55	65	
Mount Poso	20	6	2222	129	65	60	
Mount Poso	20	7	1513	142	30	30	
Mount Poso	20	8	1891	152	30	50	
Mount Poso	20	9	2411	157	255	240	
Mount Poso	20	10	6478	164	240	170	
Mount Poso	20	11	4634	163	115	115	
Mount Poso	21	1	378	98	35	35	
Mount Poso	21	2	2601	99	95	100	
Mount Poso	21	3	615	102	75	80	
Mount Poso	21	4	2506	110	130	90	
Mount Poso	21	5	1513	119	90	80	
Mount Poso	21	6	1229	129	120	65	
Mount Poso	21	7	3026	131	65	105	
Mount Poso	21	8	3121	138	105	105	
Mount Poso	21	9	3688	145	105	95	
Mount Poso	21	10	3641	144	95	90	
Mount Poso	21a	1	1229	123	0	15	
Mount Poso	21a	2	2411	128	15	50	
Mount Poso	21a	3	2459	134	50	45	
Mount Poso	21a	4	2080	139	45	30	
Mount Poso	22	1	1182	104	10	10	
Mount Poso	22	2	1324	110	10	10	
Mount Poso	22	3	1466	120	45	25	
Mount Poso	22	4	1655	120	25	15	
Mount Poso	22	5	1891	129	15	15	
Mount Poso	22	6	1797	135	15	30	
Mount Poso	22	7	2222	140	230	220	
Mount Poso	22	8	662	145	220	190	
Mount Poso	22	9	3641	142	190	185	
Mount Poso	22	10	3404	141	185	190	
Mount Poso	22	11	3073	140	345	350	
Mount Poso	22	12	3925	138	350	350	
Mount Poso	23	1	898	172	70	70	
Mount Poso	23	2	662	163	70	70	

Field	Fault Number	Segment	Length (ft)	Strike (°Clockwise from North)	Throw at the Start of Segment (ft)	Throw at the End of Segment (ft)	Note
Mount Poso	23	3	47	151	200	200	
Mount Poso	23	4	1419	148	300	300	
Mount Poso	23	5	1513	142	300	300	
Mount Poso	23	6	2411	139	300	295	
Mount Poso	23	7	4066	139	405	430	
Mount Poso	23	8	3073	139	430	430	
Mount Poso	24	1	1608	165	105	110	
Mount Poso	24	2	5390	168	110	120	
Mount Poso	24	3	1513	155	120	120	
Mount Poso	24	4	1844	147	120	125	
Mount Poso	24	5	1749	143	125	110	
Mount Poso	24	6	1229	152	110	105	
Mount Poso	24	7	1797	159	105	90	
Mount Poso	24	8	1371	160	90	70	
Mount Poso	24	9	1182	149	70	50	
Mount Poso	24	10	946	141	50	35	
Mount Poso	24	11	757	128	35	25	
Mount Poso	24	12	1229	116	80	55	
Mount Poso	24	13	1277	110	55	25	
Mount Poso	24	14	1844	115	25	30	
Mount Poso	24	15	1513	130	30	30	
Mount Poso	24	16	1371	139	30	35	
Mount Poso	24	17	1749	154	35	35	
Mount Poso	24	18	1466	163	5	5	
Mount Poso	24	19	1608	170	5	0	
Mount Poso	24	20	2648	1	0	0	
Mount Poso	25	1	1277	133	0	45	
Mount Poso	25	2	898	133	45	45	
Mount Poso	25	3	567	133	45	25	
Mount Poso	25	4	1560	133	25	0	
Mount Poso	26	1	520	172	25	25	
Mount Poso	26	2	1182	163	25	20	
Mount Poso	26	3	1088	156	20	15	
Mount Poso	26	4	1229	151	15	20	
Mount Poso	26	5	1277	148	20	20	
Mount Poso	26	6	2601	145	20	0	
Mount Poso	27	1	1513	128	235	255	
Mount Poso	27	2	993	131	255	240	
Mount Poso	28	1	3215	164	155	140	
Mount Poso	28	2	2884	167	140	130	
Mount Poso	29	1	2979	1	295	285	
Mount Poso	29	2	2553	0	285	230	
Mount Poso	29	3	2742	179	290	170	
Mount Poso	29	4	2411	177	255	235	
Mount Poso	29	5	3546	173	245	230	
Mount Poso	29	6	2175	168	230	175	
Mount Poso	30	1	378	120	45	45	
Mount Poso	30	2	1040	126	45	30	

Field	Fault Number	Segment	Length (ft)	Strike (°Clockwise from North)	Throw at the Start of Segment (ft)	Throw at the End of Segment (ft)	Note
Mount Poso	30	3	993	131	30	20	
Mount Poso	30	4	804	139	20	20	
Mount Poso	30	5	1040	148	20	15	
Mount Poso	30	6	993	160	70	90	
Mount Poso	31	1	615	141	55	55	
Mount Poso	31	2	2033	145	55	60	
Mount Poso	31	3	1702	151	60	60	
Mount Poso	31	4	1182	158	60	75	
Mount Poso	31	5	1040	168	75	85	
Mount Poso	32	1	1371	1	55	85	
Mount Poso	32	2	567	165	85	90	
Mount Poso	32	3	2411	158	90	125	
Mount Poso	32	4	1371	163	125	140	
Mount Poso	32	5	1560	166	95	110	
Mount Poso	32	6	1702	173	110	125	
Mount Poso	33	1	2175	14	110	105	
Mount Poso	33	2	1608	15	105	105	
Mount Poso	33a	1	3452	157	115	115	
Mount Poso	33a	2	2506	154	115	110	
Mount Poso	34	1	1749	177	45	30	
Mount Poso	34	2	1749	174	30	15	
Mount Poso	34	3	1419	172	15	5	
Mount Poso	34	4	1655	170	105	75	
Mount Poso	35	1	189	59	50	50	
Mount Poso	35	2	1419	59	90	90	
Mount Poso	35	3	1324	58	90	85	
Mount Poso	35	4	1054	58	85	75	
Mount Poso	35	5	236	58	65	60	
Mount Poso	35	6	426	58	20	25	
Mount Poso	36	1	1466	79	30	0	
Mount Poso	36	2	1891	79	105	185	
Mount Poso	37	1	851	60	0	20	
Mount Poso	37	2	1371	57	20	25	
Mount Poso	37	3	1324	60	25	15	
Mount Poso	37	4	1513	61	15	15	
Mount Poso	38	1	1797	43	75	70	
Mount Poso	38	2	804	42	70	50	
Mount Poso	38	3	2080	43	50	50	
Mount Poso	39	1	1040	119			
Mount Poso	40	1	757	117			
Mount Poso	41	1	2317	5	0	0	
Mount Poso	42	1	757	95	80	85	
Mount Poso	42	2	2080	99	85	90	
Mount Poso	43	1	2317	61	65	65	
Mount Poso	44	1	520	97	0	5	
Mount Poso	44	2	2317	97	5	5	
Mount Poso	45	1	851	90	90	90	
Mount Poso	45	2	1277	90	90	85	

Field	Fault Number	Segment	Length (ft)	Strike (°Clockwise from North)	Throw at the Start of Segment (ft)	Throw at the End of Segment (ft)	Note
Mount Poso	45	3	1939	91	85	100	
Mount Poso	45	4	1135	90	50	50	
Mount Poso	45	5	1324	86	50	65	
Mount Poso	45	6	851	77	65	20	
Mount Poso	45	7	1135	68	85	110	
Mount Poso	46	1	1608	76	15	40	
Mount Poso	46	2	473	74	40	35	
Mount Poso	46	3	3499	75	25	30	
Mount Poso	46	4	236	75	25	25	
Mount Poso	46	5	662	75	15	15	
Mount Poso	46	6	3404	75	25	25	
Mount Poso	47	1	1466	82	105	105	
Mount Poso	47	2	1844	80	175	195	
Mount Poso	47	3	2790	79	55	15	
Mount Poso	47	4	1844	78	15	5	
Mount Poso	47	5	804	76	20	30	
Mount Poso	48	1	1371	55	100	120	
Mount Poso	48	2	1466	58	65	60	
Mount Poso	48	3	1608	57	60	15	
Mount Poso	49	1	1182	54	0	20	
Mount Poso	49	2	709	54	20	0	
Mount Poso	50	1	2317	23	260	270	
Mount Poso	51	1	6147	98	100	100	
Mount Poso	52	1	1797	50	110	115	
Mount Poso	52	2	2601	51	115	115	
Mount Poso	53	1	520	60	0	25	
Mount Poso	53	2	1182	64	210	205	
Mount Poso	54	1	1088	60	110	120	
Mount Poso	54	2	2364	60	120	100	
Mount Poso	55	1	2459	35	85	120	
Mount Poso	55	2	2790	34	120	110	
Mount Poso	56	1	1466	64	55	55	
Mount Poso	57	1	2742	81	70	75	
Mount Poso	57	2	1797	84			
Mount Poso	58	1	1655	37	45	45	
Mount Poso	58	2	1844	44	45	45	
Mount Poso	58	3	1797	48	45	45	
Mount Poso	59	1	2648	71	660	660	
Mount Poso	59	2	2459	75	570	585	
Mount Poso	59	3	1655	78	630	625	
Mount Poso	59	4	1560	79	625	620	
Mount Poso	59	5	1135	84	620	615	
Mount Poso	59	6	1513	84	730	745	
Mount Poso	59	7	1891	88	745	765	
Mount Poso	59	8	2128	89	465	780	
Mount Poso	59	9	473	87	640	615	
Mount Poso	59	10	1182	86	455	470	
Mount Poso	59	11	1419	83	295	300	

Field	Fault Number	Segment	Length (ft)	Strike (°Clockwise from North)	Throw at the Start of Segment (ft)	Throw at the End of Segment (ft)	Note
Mount Poso	59	12	804	81	410	410	
Mount Poso	59	13	804	84	300	295	
Mount Poso	59	14	757	92	295	290	
Mount Poso	59	15	1371	99	290	295	
Mount Poso	59	16	1371	106	400	385	
Mount Poso	59	17	1844	114	385	365	
Mount Poso	59	18	1939	120	290	295	
Mount Poso	59	19	2222	121	295	300	
Mount Poso	60	1	1182	153	40	65	
Mount Poso	60	2	2175	162	175	160	
Mount Poso	61	1	1229	85	105	105	
Mount Poso	61	2	1466	75	105	100	
Mount Poso	62	1	1324	51	265	270	
Mount Poso	62	2	1277	55	270	275	
Mount Poso	62	3	1229	62	275	280	
Mount Poso	62	4	1324	71	280	300	
Mount Poso	63	1	1135	44	235	230	
Mount Poso	63	2	1324	44	230	220	
Mount Poso	63	3	1513	53	180	180	
Mount Poso	64	1	851	21	90	90	
Mount Poso	64	2	851	30	95	95	
Mount Poso	64	3	757	34	100	100	
Mount Poso	64	4	757	41	105	105	
Mount Poso	64	5	946	54	110	110	
Poso Creek	1	1	1068	118			
Poso Creek	1	2	1437	123			
Poso Creek	1	3	2358	129			
Poso Creek	1	4	847	125			
Poso Creek	1	5	2431	120	245	295	
Poso Creek	1	6	2247	123	295	330	
Poso Creek	1	7	1289	127	140	160	
Poso Creek	1	8	1768	127	160	225	
Poso Creek	1	9	1031	129	265	315	
Poso Creek	1	10	3684	126			
Poso Creek	2	1	1584	122			
Poso Creek	3	1	553	128			
Poso Creek	3	2	1510	133			
Poso Creek	3	3	921	122			
Poso Creek	4	1	1437	168	15	0	
Poso Creek	4	2	442	167	0	5	
Poso Creek	4	3	1289	164	5	25	
Poso Creek	4	4	1068	167			
Poso Creek	4	5	5489	160	20	15	
Poso Creek	4	6	626	169	15	15	
Poso Creek	4	7	553	173	15	10	
Poso Creek	4	8	663	178	10	5	
Poso Creek	4	9	921	5	5	0	
Poso Creek	5	1	1105	157	10	20	

Field	Fault Number	Segment	Length (ft)	Strike (°Clockwise from North)	Throw at the Start of Segment (ft)	Throw at the End of Segment (ft)	Note
Poso Creek	5	2	1695	155	20	0	
Poso Creek	5	3	1879	152	20	50	
Poso Creek	5	4	1510	147	50	60	
Poso Creek	5	5	1510	140	60	70	
Poso Creek	6	1	1695	177	260	230	
Poso Creek	6	2	2173	1	230	190	
Poso Creek	6	3	1584	5	190	165	
Poso Creek	6	4	1805	4	165	120	
Poso Creek	6	5	1252	178	120	85	
Poso Creek	6	6	1695	174	85	25	
Poso Creek	6	7	921	169	25	65	
Poso Creek	6	8	1363	166	65	50	
Poso Creek	6	9	1031	157	50	35	
Poso Creek	6	10	1326	149	35	20	
Poso Creek	6	11	553	160	20	15	
Poso Creek	6	12	295	169	15	20	
Poso Creek	6	13	1252	7	20	30	
Poso Creek	6	14	1068	6	30	0	
Poso Creek	6	15	1437	3	0	15	
Poso Creek	6	16	810	0	15	50	
Poso Creek	6	17	995	175	50	85	
Poso Creek	6	18	810	169	85	90	
Poso Creek	6	19	1547	163	90	105	
Poso Creek	6	20	1658	155	105	120	
Poso Creek	7	1	1473	175	40	30	
Poso Creek	7	2	1216	178	30	15	
Poso Creek	7	3	516	0	15	5	
Poso Creek	7	4	2284	0	5	95	
Poso Creek	7	5	4568	179	95	130	
Poso Creek	7	6	2836	175	130	120	
Poso Creek	7	7	2100	178	120	115	
Poso Creek	7	8	2284	0	115	65	
Poso Creek	7	9	958	0	65	70	
Poso Creek	7	10	1879	2	70	40	
Poso Creek	7	11	1289	2	40	30	
Poso Creek	7	12	1142	0	30	20	
Poso Creek	7	13	2726	0	140	140	
Poso Creek	7	14	2947	178	140	140	
Poso Creek	7	15	884	178			
Poso Creek	8	1	2394	175			
Poso Creek	8	2	2652	177			
Poso Creek	8	3	2100	178			
Poso Creek	8	4	1805	179	20	15	
Poso Creek	8	5	2984	1	15	0	
Poso Creek	9	1	1473	160			
Poso Creek	9	2	2468	165			
Poso Creek	9	3	1216	166			
Poso Creek	9	4	1252	169			

Field	Fault Number	Segment	Length (ft)	Strike (°Clockwise from North)	Throw at the Start of Segment (ft)	Throw at the End of Segment (ft)	Note
Poso Creek	9	5	1547	172			
Poso Creek	9	6	1621	175			
Poso Creek	10	1	553	85	0	10	
Poso Creek	10	2	995	85	10	10	
Poso Creek	11	1	332	112	0	10	
Poso Creek	11	2	368	112	10	10	
Poso Creek	11	3	553	112	10	0	
Poso Creek: McVan	1	1	631	118			
Poso Creek: McVan	1	2	501	125			
Poso Creek: McVan	1	3	305	132			
Poso Creek: McVan	2	1	2885	146			
Poso Creek: McVan	3	1	4268	33			
Poso Creek: McVan	4	1	446	123			
Poso Creek: McVan	5	1	4072	31			
Poso Creek: McVan	6	1	631	122			
Poso Creek: McVan	6	2	664	131			
Poso Creek: McVan	6	3	1165	141			
Poso Creek: McVan	6	4	457	147			
Poso Creek: McVan	6	5	697	154			
Poso Creek: McVan	6	6	871	161			
Poso Creek: McVan	6	7	849	163			
Poso Creek: McVan	6	8	1100	166			
Poso Creek: McVan	6	9	1285	168			
Poso Creek: McVan	7	1	980	148	70	65	
Poso Creek: McVan	7	2	588	153	65	60	
Poso Creek: McVan	7	3	490	162	60	55	
Poso Creek: McVan	7	4	1176	174	55	50	
Poso Creek: McVan	7	5	762	175	50	100	
Poso Creek: McVan	7	6	1132	177	100	85	
Poso Creek: McVan	7	7	980	178			
Poso Creek: McVan	8	1	523	130			
Poso Creek: McVan	8	2	631	139			
Poso Creek: McVan	8	3	403	145			
Poso Creek: McVan	8	4	1012	148			
Poso Creek: McVan	8	5	708	155			
Poso Creek: McVan	9	1	599	165			
Poso Creek: McVan	9	2	1644	169			
Rio Bravo	1	1	386	6			
Rio Bravo	1	2	134	6	10	5	
Rio Bravo	1	3	252	6	5	0	
Rio Bravo	1	4	185	6	0	0	
Rio Bravo	1	5	168	6	0	5	
Rio Bravo	1	6	117	6	5	0	
Rio Bravo	1	7	117	6	0	5	
Rio Bravo	1	8	654	6	5	25	
Rio Bravo	1	9	302	4	25	10	
Rio Bravo	1	10	839	4	10	5	
Rio Bravo	1	11	1426	3	5	5	

Field	Fault Number	Segment	Length (ft)	Strike (°Clockwise from North)	Throw at the Start of Segment (ft)	Throw at the End of Segment (ft)	Note
Rio Bravo	1	12	755	2	5	0	
Rio Bravo	2	1	587	3			
Rio Bravo	2	2	252	3	70	115	
Rio Bravo	2	3	235	3	115	135	
Rio Bravo	2	4	218	3	135	135	
Rio Bravo	2	5	235	3	135	145	
Rio Bravo	2	6	268	3	145	135	
Rio Bravo	2	7	336	3	135	150	
Rio Bravo	2	8	319	3	150	150	
Rio Bravo	2	9	436	3	150	140	
Rio Bravo	2	10	520	3	140	90	
Rio Bravo	2	11	872	3	90	70	
Rio Bravo	2	12	621	0	70	40	
Rio Bravo	2	13	302	0	40	25	
Rio Bravo	2	14	721	0	25	20	
Rio Bravo	2	15	755	0	20	15	
Rio Bravo	2	16	788	0	15	0	
Rio Bravo	3	1	1527	146			
Rio Bravo	3	2	1241	148			
Rio Bravo	3	3	1409	151			
Rio Bravo	3	4	1963	152			
Rosedale	1	1	1201	2			
Rosedale	1	2	1327	3	90	60	
Rosedale	1	3	1255	2	60	40	
Rosedale	1	4	1381	3	40	50	
Rosedale	1	5	1829	2			
Rosedale	2	1	2349	166			Rosedale
Rosedale	2	2	717	169			Rosedale
Rosedale	2	3	251	172			Rosedale
Rosedale	2	4	1685	178	70	100	Rosedale
Rosedale	2	5	1112	178	100	60	Rosedale
Rosedale	2	6	1506	179	60	100	Rosedale
Rosedale	2	7	484	2	100	85	Rosedale
Rosedale	2	8	520	9	85	70	Rosedale
Rosedale	2	9	520	7	215	140	Rosedale
Rosedale	2	10	377	2	140	90	Rosedale
Rosedale	2	11	412	175	90	30	Rosedale
Rosedale	2	12	914	176			Rosedale
Rosedale	2	13	753	179			Rosedale
Rosedale	3	1	484	2			Bellevue
Rosedale	3	2	663	7			Bellevue
Rosedale	3	3	2994	13			Bellevue
Rosedale	3	4	502	21			Bellevue
Rosedale	3	5	556	30			Bellevue
Rosedale	3	6	269	28			Bellevue
Rosedale	3	7	520	23			Bellevue
Rosedale	3	8	1667	2			Bellevue
Rosedale	3	9	466	178			Bellevue

Field	Fault Number	Segment	Length (ft)	Strike (°Clockwise from North)	Throw at the Start of Segment (ft)	Throw at the End of Segment (ft)	Note
Rosedale	3	10	645	171			Bellevue
Rosedale	3	11	645	165			Bellevue
Rosedale	3	12	4321	170			Bellevue
Rosedale	4	1	233	47	40	35	
Rosedale	4	2	610	47	35	25	
Rosedale	4	3	1649	47	25	10	
Rosedale	4	4	412	47	10	0	
Rosedale	5	1	2080	141	140	95	
Rosedale Ranch	1	1	396	158	30	35	
Rosedale Ranch	1	2	960	160	35	45	
Rosedale Ranch	1	3	1200	164	45	55	
Rosedale Ranch	1	4	2424	167	55	50	
Rosedale Ranch	2	1	768	1	30	30	
Rosedale Ranch	2	2	1044	5	30	30	
Rosedale Ranch	2	3	1116	9	30	30	
Rosedale Ranch	2	4	336	9	30	30	
Rosedale Ranch	2	5	636	14	25	25	
Rosedale Ranch	2	6	444	18	25	25	
Rosedale Ranch	2	7	2256	19	25	5	
Rosedale Ranch	2	8	828	20	5	0	
Rosedale Ranch	3	1	2988	164			
Rosedale Ranch	3	2	540	165			
Rosedale Ranch	3	3	444	170			
Rosedale Ranch	3	4	444	174			
Rosedale Ranch	3	5	1032	1			
Rosedale Ranch	3	6	960	4			
Rosedale Ranch	3	7	1260	5			
Rosedale Ranch	4	1	864	163			
Rosedale Ranch	4	2	720	159			
Rosedale Ranch	4	3	636	157			
Rosedale Ranch	4	4	528	159			
Rosedale Ranch	4	5	624	165			
Rosedale Ranch	4	6	720	176			
Rosedale Ranch	4	7	660	174			
Rosedale Ranch	4	8	720	177			
Rosedale Ranch	4	9	768	0			
Rosedale Ranch	4	10	744	2			
Rosedale Ranch	4	11	1092	4			
Rosedale Ranch	5	1	2280	167	40	25	
Rosedale Ranch	5	2	648	166	25	15	
Rosedale Ranch	5	3	420	169	15	5	
Rosedale Ranch	5	4	696	176	5	10	
Rosedale Ranch	5	5	708	1	10	10	
Rosedale Ranch	5	6	720	5	10	10	
Rosedale Ranch	5	7	984	7	10	10	
Rosedale Ranch	5	8	732	9	10	10	
Rosedale Ranch	5	9	924	14	10	10	
Rosedale Ranch	6	1	684	179			

Field	Fault Number	Segment	Length (ft)	Strike (°Clockwise from North)	Throw at the Start of Segment (ft)	Throw at the End of Segment (ft)	Note
Rosedale Ranch	6	2	852	2			
Rosedale Ranch	6	3	708	1			
Rosedale Ranch	6	4	588	179			
Rosedale Ranch	6	5	684	177			
Rosedale Ranch	6	6	708	171			
Rosedale Ranch	6	7	720	167			
Rosedale Ranch	6	8	612	163			
Rosedale Ranch	6	9	660	158			
Rosedale Ranch	7	1	1008	39	0	20	
Rosedale Ranch	7	2	720	41	30	10	
Rosedale Ranch	7	3	204	41	10	0	
Rosedale Ranch	7	4	216	41	0	5	
Seventh Standard	1	1	614	169	330	330	
Seventh Standard	1	2	444	175	330	330	
Seventh Standard	1	3	2476	0	330	335	
Seventh Standard	1	4	936	2	335	335	
Seventh Standard	1	5	1909	0	335	335	
Shafter	1	1	1178	143	20	20	
Shafter	1	2	1217	146	20	0	
Shafter	1	3	2552	147	0	30	
Shafter	1	4	2100	152	30	60	
Shafter	1	5	2100	156	60	90	
Shafter	1	6	2983	160	90	90	
Shafter	1	7	2316	163	90	90	
Shafter	1	8	2611	165	90	90	
Shafter Southeast Gas	1	1	6046	148			
Shafter Southeast Gas	1	2	3015	148	11	3	
Shafter Southeast Gas	1	3	3553	147	20	20	
Shafter Southeast Gas	1	4	2119	147			
Shafter Southeast Gas	2	1	5476	17	20	20	
Shafter Southeast Gas	2	2	2004	16	20	17	
Strand	1	1	3710	55			
Strand	1	2	3869	54			
Strand	1	3	4825	52			
Strand	1	4	1775	51			
Strand	2	1	1206	62	0	10	
Strand	2	2	1525	62	10	10	
Strand	2	3	956	60	10	0	
Strand	2	4	341	59	0	5	
Strand	2	5	137	59	5	0	
Strand	2	6	569	59	0	20	
Strand	2	7	1320	59	20	25	
Strand	2	8	523	59	25	25	
Strand	3	1	2390	169	90	60	
Strand	3	2	2390	169	15	20	
Strand	3	3	660	169	20	0	
Strand	3	4	273	169	0	5	
Strand	3	5	432	165	40	60	

Field	Fault Number	Segment	Length (ft)	Strike (°Clockwise from North)	Throw at the Start of Segment (ft)	Throw at the End of Segment (ft)	Note
Strand	3	6	387	165	60	35	
Strand	3	7	387	165	35	20	
Strand	3	8	660	165	20	0	
Strand	3	9	614	165	0	5	
Strand	3	10	1593	165	5	10	
Strand	3	11	910	165	10	15	
Strand	3	12	2208	165	15	20	
Strand	3	13	1616	165	20	20	
Strand	4	1	728	58	50	70	
Strand	4	2	637	58	70	50	
Strand	4	3	1024	58	50	10	
Strand	5	1	6236	152			
Strand	5	2	1206	152	5	30	
Strand	5	3	3209	152	30	10	
Strand	5	4	1730	153	10	15	
Strand	5	5	2185	153	15	5	
Strand	6	1	933	69	45	20	
Strand	6	2	592	69	20	15	
Strand	6	3	387	69	15	25	
Strand	6	4	1138	69	25	40	
Strand	7	1	1001	73			
Strand	7	2	1388	68			
Strand	7	3	1457	63			
Strand	7	4	910	59			
Strand	7	5	205	59	10	0	
Strand	7	6	205	59	0	10	
Strand	7	7	546	57	10	5	
Strand	7	8	614	55	5	5	
Strand	7	9	1001	54			
Strand	7	10	933	50			
Strand	8	1	523	125	10	15	
Strand	8	2	660	125	15	55	
Strand	8	3	546	125	55	100	
Strand	8	4	592	125	100	125	
Strand	8	5	523	125	125	145	
Strand	9	1	1161	78	0	0	
Strand	9	2	774	84	0		
Strand	9	3	1297	76			
Strand	9	4	1525	71			
Strand	9	5	1752	65		10	
Strand	9	6	1183	63	10	10	
Strand	9	7	432	60	10	10	
Strand	9	8	910	59	10	35	
Strand	9	9	1115	59	35	105	

DISCLAIMER

This document was prepared as an account of work sponsored by the United States Government. While this document is believed to contain correct information, neither the United States Government nor any agency thereof, nor The Regents of the University of California, nor any of their employees, makes any warranty, express or implied, or assumes any legal responsibility for the accuracy, completeness, or usefulness of any information, apparatus, product, or process disclosed, or represents that its use would not infringe privately owned rights. Reference herein to any specific commercial product, process, or service by its trade name, trademark, manufacturer, or otherwise, does not necessarily constitute or imply its endorsement, recommendation, or favoring by the United States Government or any agency thereof, or The Regents of the University of California. The views and opinions of authors expressed herein do not necessarily state or reflect those of the United States Government or any agency thereof or The Regents of the University of California.

Ernest Orlando Lawrence Berkeley National Laboratory is an equal opportunity employer.